



AMERICAN METEOROLOGICAL SOCIETY

Journal of Climate

EARLY ONLINE RELEASE

This is a preliminary PDF of the author-produced manuscript that has been peer-reviewed and accepted for publication. Since it is being posted so soon after acceptance, it has not yet been copyedited, formatted, or processed by AMS Publications. This preliminary version of the manuscript may be downloaded, distributed, and cited, but please be aware that there will be visual differences and possibly some content differences between this version and the final published version.

The DOI for this manuscript is doi: 10.1175/JCLI-D-16-0696.1

The final published version of this manuscript will replace the preliminary version at the above DOI once it is available.

If you would like to cite this EOR in a separate work, please use the following full citation:

Shekhar, R., and W. Boos, 2017: Weakening and Shifting of the Saharan Shallow Meridional Circulation During Wet Years of the West African Monsoon. *J. Climate.* doi:10.1175/JCLI-D-16-0696.1, in press.

© 2017 American Meteorological Society



Weakening and Shifting of the Saharan Shallow Meridional Circulation During Wet Years of the West African Monsoon

Ravi Shekhar* and William R. Boos

Yale University, New Haven, Connecticut

3

4

*Corresponding author address: Dept. of Geology and Geophysics, Yale University, P.O. Box 208109, New Haven, Connecticut.

E-mail: ravi.shekhar@yale.edu

ABSTRACT

8 The correlation between increased Sahel rainfall and reduced Saharan sur-
9 face pressure is well established in observations and global climate models,
10 and has been used to imply that increased Sahel rainfall is caused by a stronger
11 shallow meridional circulation (SMC) over the Sahara. This study uses two
12 atmospheric reanalyses to examine interannual variability of Sahel rainfall
13 and the Saharan SMC, which consists of northward near-surface flow across
14 the Sahel into the Sahara and southward flow near 700 hPa out of the Sa-
15 hara. During wet Sahel years, the Saharan SMC shifts poleward, producing a
16 drop in low-level geopotential and surface pressure over the Sahara. Statisti-
17 cally removing the effect of the poleward shift from the low-level geopotential
18 eliminates significant correlations between this geopotential and Sahel precip-
19 itation. As the Saharan SMC shifts poleward, its mid-tropospheric divergent
20 outflow decreases, indicating a weakening of its overturning mass flux. The
21 poleward shift and weakening of the Saharan SMC during wet Sahel years is
22 reproduced in an idealized model of West Africa; a wide range of imposed
23 sea surface temperature and land surface albedo perturbations in this model
24 produce a much larger range of SMC variations that nevertheless have similar
25 quantitative associations with Sahel rainfall as in the reanalyses. These re-
26 sults disprove the idea that enhanced Sahel rainfall is caused by strengthening
27 of the Saharan SMC. Instead, these results are consistent with the hypothesis
28 that the a stronger SMC inhibits Sahel rainfall, perhaps by advecting mid-
29 tropospheric warm and dry air into the precipitation maximum.

³⁰ **1. Introduction**

³¹ Over the twentieth century, large interannual and interdecadal variations in precipitation were
³² observed in the African Sahel, producing occasional floods and sustained droughts. A variety
³³ of studies examined the cause of these variations (e.g. Charney et al. 1975; Folland et al. 1986;
³⁴ Eltahir and Gong 1996; Nicholson and Grist 2001), but a robust explanation was not established
³⁵ until Giannini et al. (2003) showed that much of the observed variability could be reproduced if
³⁶ observed global SSTs were used to drive a global climate model, implicating SST as the primary
³⁷ cause of historical Sahel precipitation changes.

³⁸ While it is now generally agreed that SST drives interdecadal variations in Sahel precipitation
³⁹ (e.g. Nicholson 2013), the Sahara desert is also known to be associated with Sahel variability on a
⁴⁰ range of time scales. Haarsma et al. (2005) found a correlation on interannual time scales between
⁴¹ increased Sahel rainfall and decreased mean sea level pressure over the Sahara. They argued
⁴² that variations in the mean sea level pressure gradient between the Sahara and its surroundings
⁴³ cause variations in low-level convergence of mass and moisture, and thus in rainfall, over the
⁴⁴ Sahel. They furthermore argued that the mean sea level pressure gradient is set by the land-
⁴⁵ ocean temperature contrast, which can then be viewed as a fundamental driver of Sahel rainfall.
⁴⁶ In contrast, Biasutti et al. (2009) found that land-ocean temperature contrast is poorly correlated
⁴⁷ with Sahel precipitation at interannual time scales in CMIP3 (Coupled Model Intercomparison
⁴⁸ Project Phase 3) models. They argued that variation in Sahel rainfall is caused by fluctuations
⁴⁹ in the Saharan low, an area of near surface low pressure stretching across the Sahara desert. To
⁵⁰ quantify this, they calculated the index ΔZ_{925} , defined as the difference in geopotential height at
⁵¹ 925 hPa between the Sahara desert and the global tropics. When this index was anomalously low,
⁵² Sahel precipitation was high. Furthermore, a lead-lag correlation showed this ΔZ_{925} index was

53 maximally correlated with Sahel precipitation when the index led by one month, suggesting that
54 Saharan Low anomalies cause Sahel rainfall variability.

55 The studies just discussed treat the low-level circulation over the Sahara as an entity that can be
56 described in terms of the distribution of mean sea level pressure or 925 hPa geopotential height.
57 However, this circulation consists of a geopotential height minimum at 925 hPa over the Sahara
58 and a geopotential height maximum in the lower mid-troposphere (near 700 hPa) over the Sahara,
59 with cyclonic and anticyclonic winds rotating around the near-surface geopotential minimum and
60 the 700 hPa geopotential maximum, respectively. Fig. 1 provides a schematic of this well-known
61 structure of the Saharan circulation (e.g. Thorncroft et al. 2011). In addition to the balanced
62 cyclonic and anticyclonic flow, mass converges into the near-surface low, ascends, and diverges
63 out of the lower mid-tropospheric high in an ageostrophic overturning circulation. This shallow
64 overturning, which we refer to as the Saharan shallow meridional circulation (SMC), extends
65 across the entire Sahara desert: Fig. 2 clearly shows near-surface poleward flow across the Sahel
66 extending from the west coast of Africa to the East African highlands at nearly 40°E , with return
67 flow at 700 hPa extending over the same region (the data and methods used to create this figure
68 are described in the next section). Shallow meridional circulations have been documented over
69 Africa (Trenberth et al. 2000), in the Eastern Pacific ocean (e.g. Zhang et al. 2004; Nolan et al.
70 2007, 2010), and in the Australian monsoon (Nie et al. 2010). In continental monsoons such as
71 those in Africa, the ascent branch of the SMC is located poleward of the ascent branch of the deep,
72 precipitating intertropical convergence zone (ITCZ), whereas the ascent in the East Pacific SMC
73 is spatially coincident with the ITCZ (Zhang et al. 2008).

74 The idea that a stronger Saharan SMC causes increased Sahel precipitation in the summer mean
75 was stated explicitly by Martin and Thorncroft (2014), who examined differences in the West
76 African monsoon between warm and cold phases of the Atlantic Multidecadal Oscillation (AMO).

77 They found Sahel precipitation was enhanced during decades when the North Atlantic was warm,
78 and they stated that the Saharan SMC was stronger during the spring (April–June) immediately
79 preceding the summer rainy season (July–Sept.) of those decades. However, enhanced springtime
80 ascent in their analysis was centered over the Sahel and extended to the upper troposphere, with
81 southward flow out of that ascending region located at 600 hPa and higher altitudes; in contrast,
82 ascent in the Saharan SMC is typically confined below 600 hPa with the southward outflow cen-
83 tered at 700 hPa. Furthermore, Hurley and Boos (2013) found that 700 hPa equatorward outflow
84 from continental SMCs weakened during anomalously rainy years of the West African, southern
85 African, Australian, and South Asian monsoons. Thus, wet Sahel years seem to be characterized
86 by something other than a simple intensification of the Saharan SMC. Interpretation of the struc-
87 tures seen in the analysis of Martin and Thorncroft (2014) are complicated by the coarse resolution
88 of the NCEP-NCAR reanalysis (Kalnay et al. 1996) that they employed, which has only three to
89 four vertical levels that span the entire SMC overturning. One of our present goals is to use more
90 recent atmospheric reanalyses to describe the detailed changes in structure and intensity of the Sa-
91 haran SMC that accompany interannual changes in Sahel precipitation — interannual variability in
92 the last 30 years is expected to be better constrained by observations than interdecadal variability
93 over the last 100 years.

94 The Saharan SMC is related to the Saharan Heat Low, but the two terms describe distinct at-
95 mospheric structures. A heat low or thermal low is a warm region of the atmosphere which has
96 large thickness by the hypsometric relation; these lows are typically confined below 600 or 700
97 hPa and are sites of low surface pressure (e.g. Rácz and Smith 1999). They include the horizontal
98 balanced flow and the ageostrophic overturning circulations illustrated in Fig. 1. Although the
99 lower troposphere is hot and thus has large thickness across the entire Saharan desert, the term
100 Saharan Heat Low (SHL) is now commonly used to describe the region of maximum low-level

atmospheric thickness (LLAT) that exists over the western Sahara (e.g. Lavaysse et al. 2009), and is distinct from the Saharan Low, which is the region of low surface pressure that extends across all of northern Africa (e.g. Biasutti et al. 2009). The 700 hPa anticyclone in the upper part of the SHL is highly asymmetric, with its southward-flowing eastern branch stretching across the entire eastern half of northern Africa during summer while northward flow in its western branch is weaker and confined to the northwestern African coast (Thorncroft et al. 2011). The SMC that extends across northern Africa (e.g. Fig. 2) should thus not be thought to consist only of ageostrophic flow down the pressure gradient of the SHL, but as a combination of ageostrophic and non-divergent, balanced winds that stretches across all of northern Africa.

In the western Sahara, links between the SHL and central Sahel rainfall have been studied on a range of time scales. Lavaysse et al. (2009) showed that the SHL exhibits a pronounced seasonal cycle, and moves poleward to its boreal summer position around 20°–30°N, 7°W–5°E just before the onset of the West African monsoon, climatologically in late June. On intraseasonal and synoptic time scales, strong phases of the SHL are associated with increased moisture transport into the Sahel at low levels, accompanied by increased moisture convergence (e.g. Pu and Cook 2012) and precipitation over the central and eastern Sahel (Lavaysse et al. 2010a). Evan et al. (2015) examine the linear trend in the SHL between 1983 and 2009, showing a water vapor-forced warming of the SHL, somewhat consistent with recent work showing amplified warming over the Sahara (Vizy and Cook 2017). Lavaysse et al. (2015) show that synoptic and intraseasonal variability of the SHL can influence the seasonal-mean Sahel precipitation, although the mechanisms by which these variations influence rainfall remain unclear.

Studies of the SHL in the western Sahara (e.g. Lavaysse et al. 2010a,b) and of the Saharan Low that spans all of northern Africa (Haarsma et al. 2005; Biasutti et al. 2009) suggest that increased Sahel precipitation is caused by a decrease in Saharan surface pressure (or near surface geopo-

tential), which in turn drives an intensification of the mass flux in the Saharan SMC (Martin and Thorncroft 2014). However, some studies suggest that the sign of the association between Sahel rainfall and the Saharan SMC should be reversed, with a stronger SMC causing reduced rainfall. Peyrillé et al. (2007) and Peyrillé and Lafore (2007) used an idealized, zonally symmetric model of the West African monsoon to examine the influence on Sahel rainfall of the large-scale temperature and moisture advection produced by the Saharan SMC. They used an atmospheric reanalysis to show that the Saharan SMC produces near-surface cooling and moistening over the Sahel and Sahara, and warming and drying in the lower mid-troposphere (around 700 hPa). When they separately imposed these low- and mid-level advective tendencies in their idealized model, they found that the low-level cooling and moistening caused increased Sahel rainfall, while the mid-level warming and drying caused decreased Sahel rainfall. The effect of the mid-level warming and drying dominated, so that temperature and moisture advection in the Saharan SMC has a net inhibitory effect on Sahel rainfall. Furthermore, Zhang et al. (2008) suggested that the transport of hot and dry mid-tropospheric air into the Sahel precipitation maximum by the Saharan SMC inhibits the northward seasonal migration of the precipitation maximum during early summer. Mid-tropospheric outflow of hot and dry air from deserts has also been argued to inhibit rainfall in the Indian (Parker et al. 2016) and Australian (Xie et al. 2010) monsoons. This is consistent with the demonstrated sensitivity of precipitating convection to drying of the free troposphere above the boundary layer (Derbyshire et al. 2004; Holloway and Neelin 2009; Sobel and Schneider 2009). In summary, there is evidence for a stronger Saharan SMC having both a positive and negative influence on Sahel rainfall.

To the best of our knowledge, the observed association of interannual variations in Sahel rainfall with the detailed structure of the Saharan SMC has not been examined. It might seem reasonable to assume that the overturning in the Saharan SMC would strengthen as the near-surface Saharan

149 Low strengthens, but given the dominant effect of the mid-level warming and drying on Sahel
150 rainfall suggested by an idealized study (Peyrillé and Lafore 2007), this would be inconsistent
151 with observations of a strengthening of the near-surface Saharan Low during rainy Sahel years.
152 Perhaps low-level cooling and moistening by the Saharan SMC has a larger influence on Sahel
153 precipitation in the real world than in the idealized model of Peyrillé and Lafore (2007), similar to
154 suggestions for the role of these low-level tendencies in the observed seasonal northward migration
155 of West African rainfall (e.g. Hagos and Cook 2007; Thorncroft et al. 2011; Peyrillé et al. 2016).
156 Or perhaps the Saharan SMC does not strengthen as the near-surface Saharan Low strengthens.
157 Here we seek to resolve these questions by examining the association of Sahel rainfall with the
158 Saharan SMC at interannual timescales in two atmospheric reanalyses and an idealized model.

159 The next section of this paper describes our data sources and analysis methods. Section 3 dis-
160 cusses the climatology and basic features of the West African monsoon and Saharan SMC. Sec-
161 tion 4 examines how the horizontal structure of the near-surface Saharan Low and the Saharan
162 High covary with Sahel precipitation, and is followed by a section detailing the vertical structure
163 of the circulation changes, with emphasis on the divergent component of the flow. Section 7 com-
164 pares all of these observationally based results with output from an idealized β -plane model. We
165 close with a discussion of implications and caveats in section 8.

166 2. Methods

167 We obtain winds, geopotential height, temperature, and humidity from the ERA-Interim reanal-
168 ysis (Dee et al. 2011), which is produced by the European Centre for Medium-Range Weather
169 Forecasts (ECMWF) and is used here for 1979-2015. ERA-Interim is a third generation reanalysis
170 with data assimilation based on 12-hourly four dimensional variational analysis (4D-Var). The
171 dynamics are calculated on a T255 (approximately 80 km) global grid, with 60 vertical levels

172 from the surface to 0.1 hPa. We also use NASA's Modern-Era Retrospective analysis for Research
173 and Applications, Version 2 (MERRA2; Gelaro et al. 2017), which is a third generation reanalysis
174 produced on a $0.5^\circ \times 0.625^\circ$ cubed-sphere grid with 72 vertical levels from the surface to 0.1 hPa.
175 MERRA2 is not available for 1979, so here we use 1980-2015. All climatologies and regressions
176 shown here use ERA-Interim data unless MERRA2 is explicitly indicated. MERRA2 versions of
177 all applicable figures are provided in supplemental materials.

178 The Global Precipitation Climatology Project (GPCP) dataset (Adler et al. 2003), which is a
179 combination of land rain gauge and satellite-based precipitation measurements, is used as the
180 primary precipitation dataset for this study. The Global Precipitation Climatology Centre (GPCC,
181 Schneider et al. 2014) dataset, based on corrected gridded rain gauge data, was also examined and
182 found to produce no substantial changes in our conclusions. All data was obtained at monthly
183 mean resolution.

184 We take seasonal averages over the July-September (JAS) season for all variables, as this is
185 the peak of the Sahelian phase (e.g. Nicholson 2013) of the African monsoon. We conducted
186 a sensitivity study to alternate choices of season, specifically JJAS and JA, and found very few
187 differences in our results. The average over all JAS periods in the reanalysis time period is referred
188 to as the climatology. Fig. 3a shows the GPCP JAS climatology of precipitation, with the Sahelian
189 phase rainfall peak near 10°N .

190 We are interested in the Saharan SMC (Fig. 2), so we choose $10^\circ\text{W}-25^\circ\text{E}$ as zonal bounds
191 for our analyses. These zonal bounds encompass most of northern hemisphere Africa but ex-
192 clude coasts, the East African highlands, and the Arabian Desert. In the $10^\circ\text{W}-25^\circ\text{E}$ region,
193 the latitudes of 10°N to 20°N are defined as the Sahel, and 20°N to 30°N as the Sahara, with
194 both regions delineated with boxes in Fig. 3a. Anomalies of precipitation were calculated with
195 respect to the JAS climatology, averaging over the Sahel box and subtracting the linear trend

($0.26 \pm 0.15 \text{ mm day}^{-1} \text{ decade}^{-1}$) and the climatological mean (3.31 mm day^{-1}). The resulting timeseries is hereafter referred to as ‘Sahel precipitation’ (Fig. 3b) and forms the basis of most regressions presented here. We also removed the linear trend from all other fields regressed against this Sahel precipitation time series. We detrend for two reasons: to highlight the interannual time scale for direct comparison with previous studies (e.g. Biasutti et al. 2009), and because analyzing trends in reanalyses can be problematic due to changes in the observational network over multiple decades. In particular, Vizy and Cook (2017) show that ERA-Interim features a drying trend over the Sahel that is inconsistent with observations. Our analysis supports this view (not shown), so we restrict ourselves to the interannual time scale. The trend removed accounts for approximately 27% of the total variance in summer-mean (JAS) Sahel precipitation.

Over the reanalysis period of 1979-2015, Sahel precipitation (as measured by GPCP) lacks statistically significant interannual autocorrelations (not shown), distinguishing variability in this more recent period from the persistent interdecadal droughts that characterized parts of the twentieth century and that were largely attributed to global variations in SST (Giannini et al. 2003). Losada et al. (2012) noted the non-stationarity of the relationship between Sahel precipitation and SST in the different ocean basins over the twentieth century, and showed a marked transition in SST dependence in the 1970s, with a largely stationary regime of SST dependence since then. In our post-1970s period, precipitation variability at interannual time scales mostly exhibits a “monopole” spatial pattern (Fig. 3c), with single-signed precipitation anomalies extending from the Gulf of Guinea across the Sahel. This is in contrast to meridional “dipole” patterns of precipitation anomalies observed during the 1920s-1970s (Fig. 14 of Nicholson 2013). These monopole and dipole patterns are specific to interannual timescales, and other patterns are observed at both shorter subseasonal and longer decadal timescales. This has implications for the generality of our results, which we discuss further in section 8.

As many studies on the SHL focus on the 10°W – 10°E region, we examined the sensitivity of our results to the zonal bounds, with precipitation timeseries created by averaging over the western portion (10°W – 10°E) and eastern parts (10°E – 25°E) of the Sahel. These two timeseries were highly correlated at interannual time scales, with a coefficient of determination of $R^2 = 0.72$. Furthermore, both eastern and western Sahel precipitation timeseries were individually very highly correlated ($R^2 > 0.9$) with the precipitation timeseries presented in Fig. 3b. The entire analysis presented here was repeated for the eastern and western portions of the domain, with the appropriate eastern or western precipitation timeseries. The appendix explores some modest differences between these eastern and western subdomains, but our general conclusions also hold in these subdomains. This lack of sensitivity to the zonal bounds is consistent with the Saharan SMC (Fig. 2) and interannual variations in Sahel rainfall (Fig. 3c) being coherent across the entire zonal extent of Africa. Lavaysse et al. (2015) regress GPCP precipitation on a metric of SHL strength, in contrast to our method of regressing precipitation onto the area-averaged Sahel precipitation, and also obtain coherent rainfall anomalies across the entire Sahel (10°N – 20°N , 10°W – 25°E) at certain timescales (see their Fig. 11d). It is worth noting that Lavaysse et al. (2015) showed the positive or negative correlation between SHL strength and Sahel rainfall was timescale-dependent and zonally heterogeneous. The similarity we find between the eastern and western portions of the domain may thus not apply on timescales other than interannual.

For the idealized model portion of this study, we analyzed the same integrations presented in Shekhar and Boos (2016). These used the Weather Research and Forecasting (WRF) model, version 3.3 (Skamarock et al. 2008), modified to run on an equatorial β -plane in a meridional channel at 15 km resolution with 41 vertical levels. The domain was $20^{\circ} \times 140^{\circ}$ in the zonal and meridional directions, respectively, with periodic boundary conditions in the zonal direction and closed boundary conditions in the meridional direction. A continent was prescribed from 5°N to 32°N ,

244 divided into a grassland from 5°N–12°N and a desert from 12°N–32°N, with interactive surface
245 temperature but prescribed soil moisture and other properties from the WRF land surface database.
246 The remainder of the domain was ocean with a prescribed, idealized SST distribution representa-
247 tive of that observed during boreal summer near Africa. Perpetual July 15 insolation was imposed,
248 with the diurnal cycle retained. As shown by Xie and Saiki (1999), fixed SST, prescribed soil mois-
249 ture, and perpetual summer form a physically consistent set of simplifications, and allowing any
250 one be more realistic requires allowing all three to be more realistic to avoid unphysical variability,
251 which would greatly increase computational requirements. A total of thirteen model integrations
252 were performed for one model year after a three month spinup, yielding the same amount of output
253 for each integration as four three-month summer seasons. One integration was chosen as the con-
254 trol, and others were forced by modifications of the specified desert surface albedo, the prescribed
255 SST, or both. These form an ensemble of integrations in which the monsoon precipitation varies in
256 response to the SST and surface albedo forcings. These integrations were documented more thor-
257oughly in Shekhar and Boos (2016), where they were used to examine energy-based diagnostics
258 of ITCZ location.

259 Statistical analyses were performed using Python programming language packages Iris (U.K.
260 Met Office 2015), Seaborn (Botvinnik et al. 2016), and Statsmodels (Seabold and Perktold 2010).
261 For linear regressions, we test for a nonzero slope using a two-sided Student’s t test at the $p < 0.05$
262 level. For some linear regressions, we also obtain a 95% confidence interval for the slope using
263 a bootstrapping technique on the joint probability distribution of slope and intercept, as given in
264 the Seaborn package. We tested the sensitivity of linear regressions to outliers using the robust
265 regression (e.g. Rousseeuw and Leroy 2005) feature of the Statsmodels package, and although
266 certain confidence intervals narrow and shift slightly, no substantial qualitative differences were
267 obtained. We also examined the possibility of using nonlinear (quadratic and cubic) models for

268 regression, and found a statistical preference for nonlinear models for less than 4% of gridpoints
269 at the 95% confidence level, an amount attributable to chance.

270 **3. Basic features of the Saharan Low and SMC**

271 We begin by examining the association of interannual variations in the Saharan Low with those
272 of Sahel rainfall, then detailing the climatological mean structure of the Saharan SMC. Although
273 these analyses resemble those published previously (e.g. Biasutti et al. 2009; Thorncroft et al.
274 2011), the results confirm that the main features of interest are found in the ERA-Interim and
275 MERRA2 reanalyses and serve as a necessary reference for the rest of this paper.

276 Biasutti et al. (2009) obtained a correlation of high Sahel rainfall and negative anomalies of
277 925 hPa geopotential height (Z925) over the Sahara desert. We reproduce this correlation in re-
278 analyses (Fig. 3d). A regression of mean sea level pressure on Sahel rainfall (as in Haarsma et al.
279 2005) yields a similar pattern (not shown). These previous studies interpreted these patterns of
280 Z925 and mean sea level pressure as indicative of a strengthening of the Saharan Low. But the
281 near-surface Saharan Low stretches zonally across northern Africa and is centered around 20°N
282 while the decrease in Z925 is confined to the northern and western sides of that climatological
283 trough. Since a strengthening of the Saharan Low would consist of negative anomalies of Z925
284 centered over the climatological minimum Z925, the concentration of negative anomalies north-
285 ward and westward of that climatological minimum indicates that the Saharan Low is expanding
286 northward and westward rather than simply strengthening. Much of the northward expansion oc-
287 curs over northeastern Africa, consistent with the patterns in anomalous Z925 and mean sea level
288 pressure seen in Biasutti et al. (2009) and Haarsma et al. (2005).

289 The near-surface Saharan Low is part of the three-dimensional Saharan SMC, as mentioned in
290 the introduction. The ascending branch of the Saharan SMC is strongest at 20°N in the climatolog-

ical and zonal mean (Fig. 4a,b). An examination of the zonal structure in the appendix shows the
latitude of peak ascent moves equatorward as one moves east, from 23°N in the west to 19°N in
the east. Low level mass convergence occurs between the surface and 800 hPa, with peak conver-
gence at 925 hPa in the near-surface Saharan Low. Divergence occurs in the 800–550 hPa layer,
with peak divergence at 700 hPa associated with the Saharan High. The 925 hPa and 700 hPa
levels are taken as representative of the near-surface Saharan Low and the Saharan High, respec-
tively, in the next two sections. The maximum deep ascent in the ITCZ is located much further
south, around 8°N in ERA-Interim (Fig. 4a) and 6°N in MERRA2 (Fig. 4b). Vertical structures
of vertical velocity are somewhat different between the two reanalyses, perhaps because of dif-
ferences in convective parametrizations. There is weak time-mean divergence and subsidence in
the near-surface layer around 10°N in the precipitating region, a likely signal of strong time-mean
subsidence and sporadic ascent due to precipitation.

The near-surface zonal and meridional winds change sign around 20°N in the climatological
zonal mean (Fig. 4c,d). This change in sign, a feature sometimes described as the ITD (intertrop-
ical discontinuity), is not entirely zonally symmetric, and shifts equatorward by a few degrees
latitude as one moves eastward within our analysis domain (see section 4). Around 700 hPa, there
is a peak in the equatorward flow as air travels in the time-mean Saharan SMC toward the ITCZ.
The African Easterly Jet (AEJ; e.g. Thorncroft and Blackburn 1999) exists in thermal wind bal-
ance around 600 hPa and 14°N. At upper levels, the tropical easterly jet, meridional flow in the
upper branch of the Hadley circulation, and the midlatitude jet stream are also visible. In the next
two sections, we examine how the strength and spatial structure of the Saharan SMC covary with
Sahel precipitation.

313 **4. Horizontal structure of Saharan SMC changes**

314 Since the geopotential height and divergent wind together provide a nearly complete depiction
315 of the horizontal circulation, we start by examining the horizontal structure of geopotential and
316 divergent wind variations at 925 and 700 hPa. Fig. 5a shows the 925 hPa climatological trough
317 extending across northern Africa during JAS around 20°N. The previously discussed ITD exists
318 at the center of this trough, which shifts slightly toward the equator in the eastern portion of the
319 domain. Geostrophic flow moves cyclonically around the trough (not shown). The ageostrophic
320 winds converge into the trough, and cross-equatorial southerly flow in the low-level branch of the
321 Hadley cell is also visible over the Gulf of Guinea. When regressed on Sahel precipitation, we
322 see a spatially heterogeneous but nearly single-signed decrease in Z925 (Fig. 5b) north of 20°N
323 over northern Africa and portions of the Atlantic (the dynamical implications of this decrease are
324 discussed in the next two sections). Although changes in Z925 are not statistically significant over
325 the Sahel, there are weak anomalies of northerly divergent flow in the southern Sahel during wet
326 years that indicate a weakening of the ageostrophic northward monsoon flow at 925 hPa. At the
327 northern boundary of the Sahel, anomalous southerly wind flows across the climatological ITD
328 into the region of anomalously low Z925. Effectively, this moves the ITD and minimum of the
329 Saharan Low poleward during wet years (a quantitative measure of the meridional shift in the
330 Saharan Low is provided in the next section).

331 Fig. 5c shows the horizontal structure of the climatological mean Saharan High, with gradients
332 in Z700 in geostrophic balance with an anticyclone over most of the Saharan region. There is
333 a substantial zonal gradient in Z700 over the central and eastern Sahara, and a sharp meridional
334 gradient over the Sahel in balance with the AEJ. The peak in climatological Z700 lies poleward
335 and westward of the trough in climatological Z925. Downgradient divergent flow occurs south and

336 northwest of the 700 hPa high, constituting the divergent northerly outflow in the upper branch of
337 the Saharan SMC. The regression of Z700 onto Sahel precipitation (Fig. 5d) shows a statistically
338 significant decrease centered in the Sahel implying a strong anomalous cyclonic circulation during
339 wet years. This mid-level anomalous cyclone is also visible at 600 hPa (not shown), and is well
340 supported by observational evidence of a northward shift and weakening in the AEJ during wet
341 Sahel years (e.g. Nicholson 2013). At 700 hPa, the anomalous divergent wind converges into the
342 center of the anomalous low, around 15°N in the eastern Sahel.

343 We expect the 925 and 700 hPa surfaces to be affected differently by a strengthening of the shal-
344 low SMC compared to a strengthening of the deep, precipitating monsoon circulation. A stronger
345 shallow SMC is expected to be accompanied by a reduction in Z925 in the Saharan Low, an in-
346 crease in Z700 in the Saharan High, and an intensification of the divergent, overturning circulation
347 that flows down the geopotential gradients at these two levels. In contrast, enhanced precipitation
348 is expected to be accompanied by enhanced ascent in a deep circulation that can be approximated
349 by a first-baroclinic mode; strengthening of such a first-baroclinic mode will include decreases in
350 geopotential height in the entire lower and middle troposphere and increases in geopotential in the
351 upper troposphere [see Neelin and Zeng (2000) for a derivation of the structure of a typical tropical
352 first-baroclinic mode, and Zhang et al. (2008) or Nie et al. (2010) for illustration of how the shal-
353 low Saharan SMC coexists with a precipitating first-baroclinic mode structure over West Africa].
354 The 925 hPa and 700 hPa surfaces are thus expected to have opposite vertical displacements as
355 the Saharan SMC intensifies, simply because the Saharan LLAT would need to increase to main-
356 tain a stronger ageostrophic overturning, absent any large changes in drag. In contrast, those two
357 surfaces are both expected to move downward as the deep, precipitating circulation strengthens.
358 Fig. 5 (panels b and d) shows that the 700 and 925 hPa surfaces both move downward during
359 wet Sahel years, providing no evidence for a strengthening of the shallow SMC. Furthermore,

when geopotential heights are averaged over our Sahel and Sahara boxes, statistically significant negative anomalies in Z925 and Z700 are found during wet years in both regions (Fig. 6). Thus, geopotential variations at 925 and 700 hPa are inconsistent with the hypothesis that the Saharan SMC strengthens during wet Sahel years.

These changes in structure can also be viewed in terms of the thickness of the lower troposphere, but one must remember that LLAT will increase during a strengthening of the shallow heat low circulation and during a strengthening of the deep precipitating circulation. Shifts in the midlatitude barotropic flow (e.g. the jet stream) can also project on LLAT. The LLAT climatology (Fig. 5e) shows a maximum over the western Sahara, with relatively high LLAT extending east along the the 20°N parallel, approximately following the ITD. Thus, although the Saharan Heat Low is commonly thought of as being confined to the western Sahara (e.g. Lavaysse et al. 2009), a band of high LLAT extends eastward across the entire Sahara into the Arabian desert heat low.

The regression of LLAT onto Sahel precipitation (Fig. 5f) shows increases in LLAT centered to the northeast and northwest of our Saharan box, but the regression slope is not statistically distinct from zero over most of the Sahara. Over nearly all of the Sahel, a statistically significant decrease in the LLAT is apparent. The weak zonal variation in the anomalies shown in the right column of Fig. 5 is important: there is no thickening of the lower troposphere in the Western Sahara, where the LLAT is climatologically highest. If the Saharan Heat Low or the Saharan SMC were strengthening, we would see increased LLAT at the climatological maximum LLAT. The substantial increases in LLAT over eastern Europe, the Mediterranean, and the Atlantic might indicate interactions with the midlatitudes, perhaps through mechanisms proposed by Vizy and Cook (2009) and Lavaysse et al. (2010b). In summary, there is a decrease in LLAT on the equatorward side of the maximum LLAT, and the strong increases in LLAT are centered off the coasts of Africa, poleward of the LLAT maximum. The changes in LLAT thus seem more consistent with

384 a poleward shift, rather than a strengthening, of the thermal low and the Saharan SMC during wet
385 years. These results do not change appreciably if an alternate upper bound (e.g. 600 or 500 hPa) is
386 used to define the LLAT, which would allow us to capture a deepening of the heat low (e.g. Evan
387 et al. 2015).

388 We have thus far examined variations in geopotential height, but it is horizontal gradients in
389 geopotential that are dynamically relevant. Changes in these gradients can be assessed by eye in
390 maps of the horizontal distribution of geopotential, but we now wish to horizontally average the
391 changes in geopotential over our analysis regions. So for every JAS season we subtract the tropical-
392 mean (23°S – 23°N) geopotential height from the actual height at each pressure-level: $\Delta Z = Z -$
393 $[Z]_{\text{global tropics}}$. This methodology, which was also performed by Biasutti et al. (2009), eliminates
394 dynamically inconsequential changes in geopotential associated with tropical-mean warming or
395 cooling due to, e.g., ENSO.

396 Regressions of detrended ΔZ on Sahel precipitation quantitatively reproduce the result, shown
397 by Biasutti et al. (2009), of decreased Saharan $\Delta Z925$ during wet Sahel years (Fig. 6). The ERA-
398 Interim results are quantitatively indistinguishable from the MERRA2 results. We also see de-
399 creased $\Delta Z925$ over the Sahel, and an inspection of the climatological values (text insets in Fig. 6)
400 indicates that the meridional gradient of $\Delta Z925$ between the Sahara and Sahel flattens during wet
401 years. The Sahel LLAT decreases as a consequence of $\Delta Z925$ decreasing less than $\Delta Z700$ during
402 wet years (in this case, removal of the tropical mean has nearly zero effect, with variations in
403 $\Delta Z700 - \Delta Z925$ being nearly equal to variations in $Z700 - Z925$). This is inconsistent with the
404 idea that a classic first-baroclinic mode structure intensifies over the Sahel, and we will show in
405 the next section that the vertical profile of the anomalous convergence during wet years also differs
406 from that of a classic first-baroclinic mode, but still provides no evidence for a strengthening of
407 the Saharan low during wet years. Changes in Saharan LLAT are not statistically distinguishable

408 from zero. This analysis confirms that, even when data is horizontally averaged, no strengthening
409 of the Saharan SMC can be detected in the LLAT.

410 Since we found some evidence of a northward expansion of the Z925 trough into the Sahara
411 during wet Sahel years (Fig. 5b), we ask how much of the change geopotential can be attributed
412 to a simple meridional shift of the trough. We define the “trough latitude” by taking a 10°W–25°E
413 zonal average of $\Delta Z925$ then finding the latitude of the minimum, using cubic splines to interpolate
414 between reanalysis gridpoints. The trough latitude exhibits a modest positive correlation with
415 Sahel rainfall (Fig. 7a), with a slope of 0.50 ± 0.22 degrees mm^{-1} day in ERA-Interim. Both
416 reanalyses contain an influential data point in 1984, the driest year in the reanalysis period, with the
417 trough latitude about 1 degree farther equatorward in that year than in all other years. Removing
418 this extreme data point or using robust linear regression decreases slopes to approximately 0.45
419 degrees mm^{-1} day, but does not qualitatively change the relationship between the trough latitude
420 and Sahel precipitation. The MERRA2 data exhibit a somewhat bimodal distribution in trough
421 latitude for which we do not have an explanation.

422 The trough latitude might be influenced by changes in both the thermal low and the deep, precip-
423 itating circulation, so we also examine the latitude of the maximum zonally averaged LLAT as a
424 more direct measure of the position of the thermal low (Fig. 7b). The latitude of maximum LLAT
425 typically lies a few degrees poleward of the trough latitude and also has higher interannual vari-
426 ability. Nevertheless, it shows a northward shift of the zonally averaged thermal low during wet
427 Sahel years. The regression slopes for the 925 hPa trough latitude and the latitude of maximum
428 LLAT are statistically indistinguishable (i.e. their confidence intervals overlap).

429 We now return to the question of how much of the drop in Saharan $\Delta Z925$ can be attributed to
430 a poleward shift of the trough into the Sahara, and answer this question by statistically removing
431 the effect of this shift from the Saharan $\Delta Z925$. The regression of Saharan $\Delta Z925$ on trough lati-

tude produces a slope of -4.8 ± 2.5 meters per degree latitude (Fig. 7c). When this dependence is subtracted from the Saharan-averaged ΔZ_{925} to create a “latitude-detrended ΔZ_{925} ”, the resulting quantity has no statistically significant relationship with Sahel precipitation (Fig. 7d). This suggests that previous findings of changes in the Saharan Low during wet Sahel years (e.g. Haarsma et al. 2005; Biasutti et al. 2009) should be interpreted as a shift of the low-level trough into the Sahara. As the next section will show, many dynamic and thermodynamic quantities also show a poleward shift.

5. Vertical structure of changes in the Saharan SMC

We now examine the vertical structure of interannual variations in the West African monsoon circulation, with focus on the Saharan SMC. We first briefly examine the poleward shift of the SMC during wet monsoon years, then discuss variations in the strength of the divergent component of the circulation. While a few of the vertical structures shown here were presented in previous work (e.g. Nicholson and Grist 2001; Nie et al. 2010; Lavaysse et al. 2010a), they are included to provide a complete picture of the dynamical changes that constitute a weakening and poleward shift of the Saharan SMC.

The climatological low-level potential temperature is maximum around 22°N (Fig. 8a), poleward of the ITD. As Sahel precipitation increases, there is substantial cooling over the Sahel below 700 hPa, likely due to evaporative cooling of the land surface and reduced surface sensible heat fluxes into the boundary layer, though enhanced meridional advection of cool air into the region may also play a role poleward of 15°N where the meridional wind anomaly is positive (Fig. 8g). Above 700 hPa, warming occurs poleward of 10°N into the midlatitudes. By the hypsometric relation, this has a direct impact on the the ΔZ climatology (Fig. 8b), which shows the near surface Saharan Low centered around 18°N in the climatology and the mid-tropospheric Saharan High

455 centered around 25°N. The regression of ΔZ onto Sahel precipitation (Fig. 8b) shows that these
456 structures expand northward or shift northward at every level. The cooling of the Sahel during
457 wet years (Fig. 8a) is, by hydrostatic balance, accompanied by a thinning of the layer below
458 700 hPa and an anomalous low in the mid-troposphere (Fig. 8b). The cooling of the southern
459 part of the Saharan Low is accompanied by an increase in specific humidity (Fig. 8c) that is
460 larger, in energy units, than the decrease in temperature, so that the low-level equivalent potential
461 temperature, θ_e , is higher over the Sahel during wet years (Hurley and Boos 2013). The zonal
462 wind (Fig. 8d) has been previously reviewed in Nicholson (2013) and here we simply make the
463 point that the northward shift and weakening in the AEJ during wet years is consistent with the
464 mid-level anomalous cyclonic circulation over the Sahel shown in Fig. 5d and Fig. 8d.

465 The poleward shift in the Saharan SMC can be seen as an anomalous, meridionally asymmetric
466 quadrupole pattern in the anomalous divergence below 550 hPa (Fig. 8e; note the vertical dipole in
467 the climatological mean fields centered at 20°N). There is also a meridional expansion of the upper
468 tropospheric divergence associated with the monsoonal ITCZ. This upper tropospheric feature is
469 also visible in the vertical velocity (Fig. 8f), with more deep ascent over the Sahel during wet
470 years accompanying the anomalous dipole in low-level ascent that indicates a poleward shift in
471 the Saharan SMC. Consistent with the regression of horizontal divergence, this dipole in shallow
472 ascent is also not meridionally symmetric, with more anomalous subsidence than ascent during wet
473 years. There are also zonal asymmetries in the anomalies of shallow ascent, with the anomalous
474 subsidence near 17°N more pronounced in the western part of our domain and the anomalous
475 ascent near 22°N more pronounced in the eastern part (see Appendix).

476 The meridional wind regression (Fig. 8g) shows an asymmetric quadrupole as well, with the
477 southerly lobes of the quadrupole being spatially larger and of greater amplitude than the northerly
478 lobes. However, this asymmetry in the anomalous meridional wind should not be interpreted as a

479 weakening of the divergent circulation because we are considering a limited zonal mean, in which
480 the non-divergent component of meridional flow does not have to equal zero. When only the
481 divergent component of the meridional wind is considered (Fig. 8h), the meridional asymmetry in
482 this quadrupole is substantially reduced. But to the degree that the Saharan SMC consists of both
483 divergent and rotational components, its equatorward outflow at 700 hPa is clearly reduced during
484 wet Sahel years (Fig. 8g).

485 In the next section we better quantify interannual variations in the divergent part of the circula-
486 tion. This allows us to understand how the increased mass divergence in the upper troposphere that
487 accompanies enhanced Sahel precipitation (Fig. 8e) is compensated by increased convergence at
488 lower levels. It also allows us to assess whether asymmetries in the meridional dipoles of shallow
489 ascent and divergence are statistically significant and thus indicate a weakening of the Saharan
490 SMC.

491 **6. Changes in layer-integrated divergence**

492 The vertical section of divergence (Fig. 8e) allows identification of three layers that largely cap-
493 ture the changes in the divergent circulation: the lower troposphere (1000-800 hPa), the middle
494 troposphere (800-550 hPa), and the upper troposphere (350-100 hPa). Taking a mass-weighted
495 vertical integral of divergence over each layer (and over the remaining 550-350 hPa layer in which
496 little divergence occurs) we see the climatological signatures of the divergent Hadley circulation
497 and the Saharan SMC (Fig. 9a,c). In the lower layer, the largest convergence is due to the shallow
498 circulation; this peaks near 20°N and is stronger in ERA-Interim than in MERRA2. There is also
499 relatively weak convergence in the ITCZ near 8°N. The middle troposphere exhibits large diver-
500 gence at 20°N and substantial convergence at 10°N. Upper level divergence peaks around 8°N,
501 the latitude of maximum precipitation and deep ascent; the roughly equal magnitude and opposite

502 signs of upper-tropospheric divergence and mid-tropospheric convergence at that latitude indicate
503 that time-mean inflow to the deep, continental convergence zone occurs not near the surface but
504 in the lower mid-troposphere. There is upper level convergence poleward of about 15°N, consist-
505 ent with the northern Sahel and Sahara being regions of time-mean subsidence. Divergence in
506 the 550–350 hPa layer is comparatively small, and divergence above 100 hPa is smaller still (not
507 shown).

508 Regressing layer-integrated divergence onto Sahel precipitation (Fig. 9b,d) shows the now-
509 familiar meridional dipole indicating a poleward shift of the climatological mean divergence field
510 in the lower and mid layers, as well as a single-signed increase in upper-tropospheric divergence
511 over the Sahel region. The increase in upper tropospheric divergence indicates increased deep
512 ascent over the Sahel, consistent with precipitating convection. Near the climatological ITCZ,
513 around 8°N, upper level divergence increases little, suggesting the ITCZ is expanding northward
514 more than shifting northward. Farther north, in the shallow circulation around 20°N, the asym-
515 metry in the meridional shift is more clearly evident than in our previous depiction, with stronger
516 changes on the equatorward lobe of the dipoles, implying that the Saharan SMC weakens as it
517 shifts poleward. There are some differences between ERA-Interim and MERRA2, with the nega-
518 tive anomaly of mid-level divergence being more intense in MERRA2. Nevertheless, both reanal-
519 yses have asymmetric meridional dipoles in the anomalous lower- and mid-level divergence.

520 We wish to quantify any net change in strength of the Saharan SMC and determine if that change
521 is statistically significant after removing the effect of the northward shift. To do this, we horizon-
522 tally average the anomalous mid-level divergence over a domain large enough to encompass the
523 meridional dipoles in that field. The changes in low- and mid-level divergence associated with the
524 Saharan SMC are confined to the region between 10°N and 25°N (Figs. 8e and 9b,d). So we hori-
525 zontally average the layer-integrated divergence anomalies over 10°N–25°N, 10°W–25°E , thereby

removing the antisymmetric component of the dipole and leaving a residual that corresponds to a net strengthening or weakening of divergence in each layer over the combined Sahel-Sahara region. The 10°N bound may be located slightly too far south and thus include divergence changes associated with shifts of the ITCZ, but those changes are expected to reduce the magnitude of any signal indicative of a weakening SMC (e.g. see the low- and mid-level anomalies in Fig. 8e). Indeed, averaging over the even larger region of 5°N–25°N decreases the magnitude of the net divergence variations (which are presented below) but does not qualitatively change the result.

The result of this area-averaging of the layer-integrated divergence shows that during wet Sahel years, upper-level divergence increases, mid-level divergence decreases, and any changes in low-level divergence are not statistically distinct from zero (Fig. 10a). Layer-averaged humidity also increases (this will be further discussed in the next section). A strengthening of the Saharan SMC would consist of a decrease in low-level divergence (enhanced convergence), and an increase in mid-level divergence; our area-averaged results have the opposite sign at mid-levels. Furthermore, Fig. 10b shows mid-level divergence is strongly anticorrelated with upper-level divergence, indicating that the enhanced upper-tropospheric divergence during wet monsoon years is balanced, in the summer-mean column mass budget, by decreased mid-tropospheric divergence. This balance is quantitatively confirmed by the fact that the regression coefficient relating upper- and mid-level layer-integrated convergence is approximately -1. Interannual variations in the deep, precipitating monsoon circulation thus cannot be captured by a classic first-baroclinic mode that has maximum convergence near the surface and divergence at upper levels. Thorncroft et al. (2011) showed that the climatological mean moisture flux convergence in the Sahel has a complicated vertical structure with a weak maximum in our mid-tropospheric layer associated with flow in the Saharan SMC, so it is perhaps not surprising that variations in the flow also do not have a simple clas-

549 sical structure. This issue is discussed further in the next section in the context of our idealized
550 simulations.

551 7. Model of a weakening and shifting Saharan SMC

552 Our idealized WRF model integrations, performed at 15 km horizontal resolution on a zonally
553 periodic β -plane, are detailed in section 2 and in Shekhar and Boos (2016). A variety of surface
554 albedo and SST forcings were applied individually about a control state to form an ensemble of
555 model integrations. Instead of examining interannual variability within individual integrations,
556 we look at the intra-ensemble variability of the long-term time-mean state and compare it to in-
557 terannual variability within the reanalyses. Due to the zonally symmetric boundary conditions
558 of the idealized model, the time-mean zonal wind is non-divergent and there are no large scale
559 dynamical forcings such as those associated with ENSO or the South Asian monsoon, which
560 could produce differences between observed interannual variability and the model intra-ensemble
561 variability. Nevertheless, we find quantitative similarities in the statistical association between
562 simulated monsoon precipitation and multiple dynamical variables.

563 The ensemble members are strongly forced (e.g. Saharan albedo changes of 0.1 to 0.2), so rep-
564 resent a wider range of ITCZ and SMC locations than is observed in the modern historical record.
565 After a spinup period, each ensemble member produces a different climatological state (averaged
566 over four three-month summer seasons) in response to the applied perturbations. Fig. 11 shows
567 how the time-mean mass streamfunction (obtained using the method of Döös and Nilsson 2011)
568 changes between integrations having the driest Sahel and those with the wettest Sahel (the model
569 Sahel is also defined as the region 10–20°N). In the ensemble member with the lowest precipita-
570 tion, deep ascent peaks at 8°N and ascent in the SMC is well separated with a peak at 17°N. In this
571 state, the summer Hadley cell is strong, the cross-equatorial winter Hadley cell is relatively weak,

and the SMC is relatively strong. As precipitation increases over the Sahel box (e.g. Fig. 11c), the ITCZ moves poleward into continent, the winter Hadley cell strengthens, the summer Hadley cell weakens, and the separation between the SMC ascent and the ITCZ decreases. As Sahel precipitation increases further (e.g. Fig. 11e), the winter Hadley cell continues to strengthen, the summer Hadley cell continues to weaken, and the shallow SMC ascent begins to merge with the ITCZ.

Quantitatively comparing our idealized model with observations is complicated by the task of choosing an appropriate region over which to average precipitation and divergence. In the reanalyses, the Sahel (10°N – 20°N) always lies on the poleward edge of the ITCZ and the ascending branch of the Saharan SMC is centered in the region over which we averaged divergence (10°N – 25°N). In the idealized model, the ITCZ and SMC move over a much wider latitude band, with the ITCZ centered south of the averaging region in some integrations and squarely within it in others (Fig. 11). Nevertheless, ascent in the model SMC always lies between 10°N and 25°N , so variations in the strength of mid-tropospheric divergence produced by the Saharan SMC should be well captured by averages of the layer-integrated divergence between those latitude bounds. For this reason, we average precipitation and layer-integrated divergence over the same regions chosen for the reanalyses.

As expected, the observed interannual variability of both Sahel precipitation and SMC latitude is much smaller than variability in the model ensemble (Fig. 12a). There is quantitative agreement between the regression coefficients based on observed and simulated variables: the 95% confidence interval for the slope of model Sahel precipitation regressed on model SMC latitude overlaps with that of both ERA-Interim and MERRA2. The idealized model also exhibits associations between Sahel precipitation and upper-level divergence, mid-level convergence, and area-averaged, layer-integrated humidity that are quantitatively similar to those seen in observed interannual variability (Fig. 12b). This agreement is remarkable given that the model was not

596 tuned to observed interannual variability: these simulations were performed for a different study
597 (Shekhar and Boos 2016) that was completed before this analysis was undertaken. However, the
598 idealized model disagrees with observations in that it simulates enhanced low-level convergence
599 when there is enhanced Sahel precipitation (recall that the reanalyses indicate a weak reduction of
600 low-level convergence during anomalously rainy years). Enhanced precipitating ascent in the ide-
601 alized model thus seems to be better described by a classic first-baroclinic mode vertical structure
602 than in reanalyses. Whether this means that the model is unsuitable for representing interactions
603 between the monsoonal ITCZ and the Saharan SMC is unclear, in large part because there has been
604 little study of the implications of deviations from a first-baroclinic mode structure for variability
605 in monsoons.

606 Despite some bias in its simulation of the vertical structure of the ITCZ, this idealized model
607 clearly simulates a weakening and poleward shift of the Saharan SMC circulation in states with
608 enhanced Sahel precipitation. Furthermore, the model results suggest that the circulation over
609 West Africa exists on a continuum. At one end of the continuum, dry states have a coastal ITCZ
610 close to the equator, large separation between the ITCZ and ascent in the SMC, and a strong
611 Saharan SMC circulation with abundant mid-tropospheric divergence. At the other end of the
612 continuum, the ITCZ is positioned much further poleward in a continental location, the winter
613 Hadley cell is stronger while the summer Hadley cell is weaker, and the overturning mass flux and
614 mid-tropospheric divergence in the Saharan SMC are weaker. In that state, which is an idealized
615 analogue of observed wet-Sahel years, the ascending branches of the SMC and ITCZ have begun
616 to merge to produce a vertical structure closer to that of first-baroclinic mode ascent common in
617 deep convective regions.

618 **8. Discussion**

619 Previous work found intriguing associations between Sahel precipitation and the strength of both
620 the Saharan Low that stretches across Africa and the SHL in the western Sahara. At interannual
621 and longer times scales, an enhancement of either the Saharan Low or the SHL is associated with
622 increased rainfall over the Sahel (e.g. Haarsma et al. 2005; Biasutti et al. 2009; Lavaysse et al.
623 2015, section 4). However, previous studies did not examine the detailed changes in the three-
624 dimensional lower-tropospheric circulation that stretches across northern Africa — the Saharan
625 SMC. Martin and Thorncroft (2014) argued that a strong springtime shallow meridional circula-
626 tion across West Africa accompanied enhanced summer rainfall over the Sahel during decades
627 when the North Atlantic was anomalously warm. They claimed that “the intensified shallow
628 meridional overturning circulation increases moisture flux into the Sahel from the south during
629 spring”, describing a mechanism in which an intensified mass flux in an SMC causes enhanced
630 Sahel rainfall.

631 Here we find the changes in lower-tropospheric winds and geopotential during wet Sahel years
632 are best described as a poleward shift and weakening of the Saharan SMC. At low levels, the
633 decrease in geopotential was located north of the climatological mean geopotential minimum,
634 suggesting a northward expansion or shift, rather than an intensification, of the low-level trough
635 during wet monsoon years. When the linear relationship between the 925 hPa trough latitude
636 and Sahel precipitation was statistically removed, effectively subtracting the poleward shift of the
637 Saharan Low from the geopotential field, no statistically significant relationship remained between
638 Sahel precipitation and Saharan 925 hPa geopotential.

639 Our analyses of ascent and horizontal divergence showed that the divergent component of the
640 Saharan SMC weakened and shifted poleward during wet Sahel years. Upper tropospheric di-

vergence over the Sahel increased during wet years, as expected for a deep, precipitating monsoon circulation. Shallow ascent in the Saharan SMC shifted poleward and weakened during wet years, as evidenced by the meridionally asymmetric dipole of anomalous vertical velocity in the lower troposphere over the Sahara (Fig. 8f). Asymmetric meridional dipoles were also seen in the divergence integrated over the lower and middle troposphere, confirming this weakening and poleward shifting of the shallow circulation. The increased upper-level divergence during wet years is balanced, in the column integrated mass budget, by decreased divergence in the lower mid-troposphere, indicating some departure from classic first-baroclinic mode structures that have maximum convergence near the surface. Nevertheless, these results suggest a trade-off between the shallow and deep modes of vertical ascent, where unusually wet years exhibit a stronger deep circulation and weaker Saharan SMC.

An idealized model of the West African monsoon was used to produce an ensemble of integrations forced by applied SST and land surface albedo anomalies. This ensemble explores a variety of climatic states with a much greater range than that of interannual variations in reanalyses. Nevertheless, without any tuning, the intra-ensemble variability of the idealized model climatological means exhibits a similar relationship between the Saharan SMC and Sahel precipitation seen in observed interannual variability. Increases in deep, precipitating ascent in the model were better described by a classic first-baroclinic mode than they were in reanalyses, but both the model and the reanalyses clearly showed a weakening of mid-tropospheric divergence in the Saharan SMC as monsoon precipitation increased.

All of this supports the hypothesis that the Saharan SMC inhibits, rather than strengthens, Sahel precipitation. This is consistent with the results of Peyrillé and Lafore (2007), who showed that dry and warm outflow from the Saharan high weakened Sahel precipitation in another idealized model, and that this weakening was stronger than any strengthening produced by an enhanced poleward

moisture flux at low levels in the SMC. As mentioned in the introduction, Zhang et al. (2008) also suggested that mid-level warming and drying by SMC outflow inhibits the northward progression of Sahel rainfall during early summer. Studies of other monsoon regions have also provided evidence that a stronger SMC causes weaker monsoon rainfall: Xie et al. (2010) established a relationship between mid-level advective drying and reduced rainfall on intraseasonal time scales in the Australian monsoon, while Parker et al. (2016) showed that the summer onset of monsoon rains is accompanied by the weakening of mid-level advective drying. Although our observational results do not establish causation in the association between Sahel rainfall and the strength and location of the Saharan SMC, they do disprove the hypothesis that increased Sahel precipitation is caused by a strengthening of the that SMC. In our idealized model, the ultimate cause of changes in precipitation was anomalies in SST and land surface albedo, but variations in the Saharan SMC could be part of the mechanism by which those forcings influence Sahel precipitation.

A few major caveats are worth noting. First, we focus on interannual variations of Sahel precipitation with the linear trend removed. As Lavaysse et al. (2015) show, at subseasonal and decadal timescales, the relationship between Sahel precipitation and the near-surface Saharan Low is zonally heterogeneous, whereas we take largely a zonal mean approach to analyze the Saharan SMC. Second, we remove the long term trends primarily for reasons of data quality, and there may be interesting trends in the SMC that we cannot detect. Third, Fig. 3c showed that variations in GPCP precipitation exhibit a “monopole” pattern over West Africa since 1979 on interannual timescales. The reanalysis precipitation fields in ERA-Interim and MERRA-2 show more of a dipole pattern of interannual variability over this period, with a statistically significant decrease in precipitation over the Gulf of Guinea ($5\text{--}10^{\circ}\text{N}$) during wet Sahel years (not shown). This dipole pattern of precipitation anomalies, which is consistent with a meridional shift of the ITCZ and which characterized rainfall variations earlier in the twentieth century (Losada et al. 2012), has not been seen

in precipitation measurements after the 1970s. So it seems possible that the reanalyses are representing a biased spatial pattern of precipitation variability during the past few decades, assuming the precipitation observations are not themselves in error. This uncertainty in precipitation over the coastal Gulf of Guinea region influenced our decision to use 10°N as the southern boundary when calculating area averaged, layer integrated divergence, so that this uncertain region is excluded. Even if the reanalyses have a biased representation of interannual variability in this region, it seems unlikely that this is large enough to change our broad conclusions (e.g. the sign of correlations between Sahel precipitation and geopotential height, divergence, and Saharan ascent would need to be wrong in two reanalysis products). Confirmation of some of these associations in an idealized model lends further confidence to our results. Nevertheless, it is good to bear in mind that reanalyses have bias, even while they remain a useful tool for understanding historical atmospheric variability over the last few decades.

Important questions remain. Does the association between a weak Saharan SMC and increased Sahel rainfall result from a time-average of a similar association on intraseasonal or synoptic time scales? Answering this question is complicated by the fact that recent studies of subseasonal variability of the Saharan circulation have focused on selecting periods when the regional maximum of LLAT over northwest Africa (i.e. the darkest green shading in Fig. 5e) had an extreme value (Lavaysse et al. 2009, 2010a,b). This approach tends to select periods with strong near-surface cyclonic flow west of the dateline; the concurrent precipitation anomalies are positive over the Gulf of Guinea and the central Sahel but negative over the far western Sahel. That pattern of anomalous rainfall is distinct from the nearly zonally symmetric structure seen when the rainfall itself is used to create composites or regressions (e.g. Fig. 3c). Vizy and Cook (2014) documented an association between surges of cold air across the Sahara and reduced precipitation over the eastern Sahel on both intraseasonal and interannual time scales, but the spatial structures of the

713 precipitation and dynamical anomalies associated with those cold surges were very different from
714 those of the anomalies we studied here. Although the mechanisms of subseasonal variability are
715 important, there is a long tradition of using two-dimensional models of atmospheric meridional
716 overturning circulations to represent the seasonal mean West African monsoon (e.g. Charney et al.
717 1975; Zheng and Eltahir 1998). Our results disprove the idea a stronger Saharan SMC causes
718 enhanced Sahel rainfall in the summer mean (e.g. Martin and Thorncroft 2014), and are instead
719 consistent with the idea that the SMC inhibits Sahel rainfall by mixing dry air into that region.

720 *Acknowledgments.* Both authors were supported by National Science Foundation grant AGS-
721 1253222. This work was supported in part by the facilities and staff of the Yale University Faculty
722 of Arts and Sciences High Performance Computing Center. Computing support was also provided
723 by Yellowstone (ark:/85065/d7wd3xhc), supported by NCAR’s Computational and Information
724 Systems Laboratory. We would also like to thank Xavier Levine for many fruitful discussions.

725 APPENDIX

726 Recent work has focused on the relationship between the Saharan Heat Low in the western Sa-
727 hara and its relationship to precipitation over the Sahel Lavaysse et al. (e.g. 2015). In section 4,
728 we show there is also a region of enhanced LLAT in the eastern Sahara, extending along the 20°N
729 parallel (Fig. 5e). Although, this feature in the eastern Sahara is not commonly called the SHL –
730 that term seems to be reserved for the heat low in the western Sahara — a heat low circulation is
731 nevertheless present in the eastern Sahara (Fig. 8a, b). This circulation includes an SMC marked
732 by near surface horizontal convergence, shallow ascent, and mid-level horizontal divergence. In
733 the western Sahara, the shallow ascent extends from approximately 15–25°N, while in the east-
734 ern Sahara it is more meridionally confined, extending from approximately 14–22°N. The deep
735 circulation also exhibits some zonal inhomogeneity: as one moves east across Africa, the ITCZ

shifts closer to the equator and is associated with more intense and meridionally broader ascent.
The ITD, as measured by the zero in near-surface meridional wind (Fig. 8c, d) also moves toward
the equator as one moves east. This is consistent with the slight tilt of the low-level geopotential
trough shown in Fig. 5a.

Fig. 8 shows dynamical fields zonally averaged over the western and the eastern parts of our analysis domain regressed on our standard Sahel precipitation time series; no meaningful differences are found when using precipitation indices derived separately from the eastern and western portions of the domain (not shown). Regressions of horizontal divergence (Fig. 8a, b) show the SMC shifts north in both the eastern and western portions of the domain, but the shift is more pronounced and statistically significant in the eastern portions of the domain. In contrast, the western part of the domain exhibits more of a weakening of the southern half of the SMC. Regressions of pressure velocity (Fig. 8c, d) show essentially the same picture, with the SMC shift showing a dipole in both eastern and western regions, but anomalous subsidence dominating the western region and ascent dominating the eastern region. This shows that if one were to consider the western region alone, the region with the SHL, wet years would be associated with a decrease in the upward shallow mass flux in the SHL. Thus, our conclusion that the SMC weakens during wet Sahel years becomes even stronger when one limits the analysis to the western part of our domain. Averaging over a broader zonal region makes the meridional dipole in anomalous shallow ascent (Fig. 8f) show greater meridional antisymmetry.

There is a great deal of similarity between the zonal wind anomalies in the eastern and western regions (Fig. 8e, f), although the barotropic subtropical jet seems to change more in the western region. The southward wind at 700 hPa (the top of the SMC) is stronger in the eastern domain because that region lies on the eastern edge of the 700 hPa anticyclone (Fig. 8g, h); the southward

759 700 hPa wind over the Sahel weakens more in the eastern region during wet years, providing yet
760 another indicator of the weakening of the entire shallow circulation over the Sahara.

761 **References**

- 762 Adler, R. F., and Coauthors, 2003: The Version-2 Global Precipitation Climatology Project
763 (GPCP) Monthly Precipitation Analysis (1979 - Present). *Journal of Hydrometeorology*, **4** (6),
764 1147–1167, doi:10.1175/1525-7541(2003)004<1147:TGPCP>2.0.CO;2.
- 765 Biasutti, M., A. H. Sobel, and S. J. Camargo, 2009: The Role of the Sahara Low in Summertime
766 Sahel Rainfall Variability and Change in the CMIP3 Models. *Journal of Climate*, **22** (21), 5755–
767 5771, doi:10.1175/2009JCLI2969.1.
- 768 Botvinnik, O., and Coauthors, 2016: seaborn: v0.7.0 (January 2016). URL <https://github.com/mwaskom/seaborn>, doi:10.5281/zenodo.45133.
- 770 Charney, J., P. H. Stone, and W. J. Quirk, 1975: Drought in the Sahara: A Biogeophysical Feed-
771 back Mechanism. *Science*, **187** (4175), 434–435, doi:10.1126/science.187.4175.434.
- 772 Dee, D. P., and Coauthors, 2011: The ERA-Interim reanalysis: Configuration and performance of
773 the data assimilation system. *Quarterly Journal of the Royal Meteorological Society*, **137** (656),
774 553–597, doi:10.1002/qj.828.
- 775 Derbyshire, S., I. Beau, P. Bechtold, J.-Y. Grandpeix, J.-M. Piriou, J.-L. Redelsperger, and
776 P. Soares, 2004: Sensitivity of moist convection to environmental humidity. *Quarterly Journal of the Royal Meteorological Society*, **130** (604), 3055–3079, doi:10.1256/qj.03.130.
- 778 Döös, K., and J. Nilsson, 2011: Analysis of the Meridional Energy Transport by Atmospheric
779 Overturning Circulations. *Journal of the Atmospheric Sciences*, **68** (8), 1806–1820, doi:
780 10.1175/2010JAS3493.1.

- 781 Eltahir, E. a. B., and C. Gong, 1996: Dynamics of wet and dry years in West Africa. *Journal of*
782 *Climate*, **9** (5), 1030–1042, doi:10.1175/1520-0442(1996)009<1030:DOWADY>2.0.CO;2.
- 783 Evan, A. T., C. Flamant, C. Lavaysse, C. Kocha, and A. Saci, 2015: Water Vapor Forced Green-
784 house Warming over the Sahara Desert and the Recent Recovery from the Sahelian Drought.
785 *Journal of Climate*, **28**, 108–123, doi:10.1175/JCLI-D-14-00039.1.
- 786 Folland, C. K., T. N. Palmer, and D. E. Parker, 1986: Sahel rainfall and worldwide sea tempera-
787 tures, 1901–85. *Nature*, **320** (6063), 602–607, doi:10.1038/320602a0.
- 788 Gelaro, R., and Coauthors, 2017: The modern-era retrospective analysis for research and applica-
789 tions, version 2 (merra-2). *Journal of Climate*, **(2017)**.
- 790 Giannini, A., R. Saravanan, and P. Chang, 2003: Oceanic forcing of Sahel rainfall on interannual
791 to interdecadal time scales. *Science*, **302** (5647), 1027–30, doi:10.1126/science.1089357.
- 792 Haarsma, R. J., F. M. Selten, S. L. Weber, and M. Kliphuis, 2005: Sahel rainfall variability and
793 response to greenhouse warming. *Geophysical Research Letters*, **32** (1), 17 702, doi:10.1029/
794 2005GL023232.
- 795 Hagos, S. M., and K. H. Cook, 2007: Dynamics of the West African monsoon jump. *Journal of*
796 *Climate*, **20** (21), 5264–5284, doi:10.1175/2007JCLI1533.1.
- 797 Holloway, C., and J. D. Neelin, 2009: Moisture vertical structure, column water vapor, and tropical
798 deep convection. *Journal of the Atmospheric Sciences*, doi:10.1175/2008JAS2806.1.
- 799 Hurley, J. V., and W. R. Boos, 2013: Interannual Variability of Monsoon Precipitation and Local
800 Subcloud Equivalent Potential Temperature. *Journal of Climate*, **26**, 9507–9527, doi:10.1175/
801 JCLI-D-12-00229.1.

- 802 Kalnay, E., and Coauthors, 1996: The NCEP/NCAR 40-Year Reanalysis Project. *Bulletin of the*
803 *American Meteorological Society*, **77** (3), 437–471, doi:10.1175/1520-0477(1996)077<0437:
804 TNYRP>2.0.CO;2.
- 805 Lavaysse, C., C. Flamant, A. Evan, S. Janicot, and M. Gaetani, 2015: Recent climatological trend
806 of the Saharan heat low and its impact on the West African climate. *Climate Dynamics*, doi:
807 10.1007/s00382-015-2847-z.
- 808 Lavaysse, C., C. Flamant, and S. Janicot, 2010a: Regional-scale convection patterns during strong
809 and weak phases of the Saharan heat low. *Atmospheric Science Letters*, **11** (4), 255–264.
- 810 Lavaysse, C., C. Flamant, S. Janicot, and P. Knippertz, 2010b: Links between African easterly
811 waves, midlatitude circulation and intraseasonal pulsations of the West African heat low. *Quar-*
812 *terly Journal of the Royal Meteorological Society*, **136** (1), 141–158, doi:10.1002/qj.555.
- 813 Lavaysse, C., C. Flamant, S. Janicot, D. J. Parker, J. P. Lafore, B. Sultan, and J. Pelon, 2009: Sea-
814 sonal evolution of the West African heat low: A climatological perspective. *Climate Dynamics*,
815 **33** (2-3), 313–330, doi:10.1007/s00382-009-0553-4.
- 816 Losada, T., B. Rodriguez-Fonseca, E. Mohino, J. Bader, S. Janicot, and C. R. Mechoso, 2012:
817 Tropical SST and Sahel rainfall: A non-stationary relationship. *Geophysical Research Letters*,
818 **39** (12), 1–7, doi:10.1029/2012GL052423.
- 819 Martin, E. R., and C. D. Thorncroft, 2014: The impact of the AMO on the West African monsoon
820 annual cycle. *Quarterly Journal of the Royal Meteorological Society*, **140** (678), 31–46, doi:
821 10.1002/qj.2107.

- 822 Neelin, J. D., and N. Zeng, 2000: A Quasi-Equilibrium Tropical Circulation Model{–
823 }Formulation*. *Journal of the Atmospheric Sciences*, **57** (11), 1741–1766, doi:10.1175/
824 1520-0469(2000)057<1741:AQETCM>2.0.CO;2.
- 825 Nicholson, S., and J. Grist, 2001: A conceptual model for understanding rainfall variability in
826 the West African Sahel on interannual and interdecadal timescales. *International Journal of*
827 *Climatology*, **21** (14), 1733–1757, doi:10.1002/joc.648.
- 828 Nicholson, S. E., 2013: The West African Sahel: A Review of Recent Studies on the Rainfall
829 Regime and Its Interannual Variability. *ISRN Meteorology*, **2013** (4), 1–32, doi:10.1155/2013/
830 453521.
- 831 Nie, J., W. R. Boos, and Z. Kuang, 2010: Observational Evaluation of a Convective Quasi-
832 Equilibrium View of Monsoons. *Journal of Climate*, **23** (16), 4416–4428, doi:10.1175/
833 2010JCLI3505.1.
- 834 Nolan, D. S., S. W. Powell, C. Zhang, and B. E. Mapes, 2010: Idealized Simulations of the
835 Intertropical Convergence Zone and Its Multilevel Flows. *Journal of the Atmospheric Sciences*,
836 **67** (12), 4028–4053, doi:10.1175/2010JAS3417.1.
- 837 Nolan, D. S., C. Zhang, and S.-h. Chen, 2007: Dynamics of the Shallow Meridional Circulation
838 around Intertropical Convergence Zones. *Journal of the Atmospheric Sciences*, **64** (7), 2262–
839 2285, doi:10.1175/JAS3964.1.
- 840 Parker, D. J., P. Willetts, C. Birch, A. G. Turner, J. H. Marsham, C. M. Taylor, S. Korusu, and
841 G. M. Martin, 2016: The interaction of moist convection and mid-level dry air in the advance
842 of the onset of the Indian monsoon. *Quarterly Journal of the Royal Meteorological Society*,
843 **142** (699), 2256–2272, doi:10.1002/qj.2815.

- 844 Peyrillé, P., and J.-P. Lafore, 2007: An Idealized Two-Dimensional Framework to Study the West
845 African Monsoon. Part II: Large-Scale Advection and the Diurnal Cycle. *Journal of the Atmo-*
846 *spheric Sciences*, **64** (8), 2783–2803, doi:10.1175/JAS4052.1.
- 847 Peyrillé, P., J.-P. Lafore, and A. Boone, 2016: The annual cycle of the West African monsoon
848 in a two-dimensional model: mechanisms of the rain-band migration. *Quarterly Journal of the*
849 *Royal Meteorological Society*, **142** (696), 1473–1489, doi:10.1002/qj.2750.
- 850 Peyrillé, P., J.-P. Lafore, and J.-L. Redelsperger, 2007: An Idealized Two-Dimensional Framework
851 to Study the West African Monsoon. Part I: Validation and Key Controlling Factors. *Journal of*
852 *the Atmospheric Sciences*, **64** (8), 2765–2782, doi:10.1175/JAS3919.1.
- 853 Pu, B., and K. H. Cook, 2012: Role of the West African Westerly Jet in Sahel Rainfall Variations.
854 *Journal of Climate*, **25** (8), 2880–2896, doi:10.1175/JCLI-D-11-00394.1.
- 855 Rácz, Z., and R. K. Smith, 1999: The dynamics of heat lows. *Quarterly Journal of the Royal*
856 *Meteorological Society*, **125** (553), 225–252, doi:10.1002/qj.49712555313.
- 857 Rousseeuw, P. J., and A. M. Leroy, 2005: *Robust regression and outlier detection*, Vol. 589. John
858 Wiley & Sons.
- 859 Schneider, T., T. Bischoff, and G. H. Haug, 2014: Migrations and dynamics of the intertropical
860 convergence zone. *Nature*, **513** (7516), 45–53, doi:10.1038/nature13636.
- 861 Seabold, J., and J. Perktold, 2010: Statsmodels: Econometric and statistical modeling with python.
862 *Proceedings of the 9th Python in Science Conference*.
- 863 Shekhar, R., and W. R. Boos, 2016: Improving Energy-Based Estimates of Monsoon Location
864 in the Presence of Proximal Deserts. *Journal of Climate*, **29** (13), 4741–4761, doi:10.1175/
865 JCLI-D-15-0747.1.

- 866 Skamarock, W. C., and Coauthors, 2008: A description of the advanced research WRF version 3.
867 *NCAR technical note.*
- 868 Sobel, A. H., and T. Schneider, 2009: Single-layer axisymmetric model for a Hadley circulation
869 with parameterized eddy momentum forcing. *Journal of Advances in Modeling Earth Systems*,
870 **2**, 10.
- 871 Thorncroft, C. D., and M. Blackburn, 1999: Maintenance of the African easterly jet. *Quarterly*
872 *Journal of the Royal Meteorological Society*, **125 (555)**, 763–786, doi:10.1002/qj.49712555502.
- 873 Thorncroft, C. D., H. Nguyen, C. Zhang, and P. Peyrillé, 2011: Annual cycle of the West African
874 monsoon: regional circulations and associated water vapour transport. *Quarterly Journal of the*
875 *Royal Meteorological Society*, **137 (654)**, 129–147, doi:10.1002/qj.728.
- 876 Trenberth, K. E., D. P. Stepaniak, and J. M. Caron, 2000: The Global Monsoon as Seen through
877 the Divergent Atmospheric Circulation. *Journal of Climate*, **13 (22)**, 3969–3993, doi:10.1175/1520-0442(2000)013<3969:TGMAS>2.0.CO;2.
- 878 U.K. Met Office, 2015: *Iris: A Python library for analysing and visualising meteorological and*
879 *oceanographic data sets*. Exeter, Devon, v1.8 ed., URL <http://scitools.org.uk/>.
- 880 Vizy, E. K., and K. H. Cook, 2009: A mechanism for African monsoon breaks: Mediterranean
881 cold air surges. *Journal of Geophysical Research: Atmospheres*, **114 (1)**, 1–19, doi:10.1029/2008JD010654.
- 882 Vizy, E. K., and K. H. Cook, 2014: Impact of cold air surges on rainfall variability in the Sahel
883 and wet African tropics: a multi-scale analysis. *Climate Dynamics*, **43 (3-4)**, 1057–1081, doi:
884 10.1007/s00382-013-1953-z.

- 887 Vizy, E. K., and K. H. Cook, 2017: Seasonality of the observed amplified sahara warming trend
888 and implications for sahel rainfall. *Journal of Climate*, **30** (9), 3073–3094.
- 889 Xie, S.-P., C. Deser, G. A. Vecchi, J. Ma, H. Teng, and A. T. Wittenberg, 2010: Global Warming
890 Pattern Formation: Sea Surface Temperature and Rainfall*. *Journal of Climate*, **23** (4), 966–
891 986, doi:10.1175/2009JCLI3329.1.
- 892 Xie, S.-P., and N. Saiki, 1999: Abrupt onset and slow seasonal evolution of summer monsoon in
893 an idealized GCM simulation. *Journal of the Meteorological Society of Japan*, **77**, 949–968.
- 894 Zhang, C., M. McGauley, and N. A. Bond, 2004: Shallow Meridional Circulation in the Tropical
895 Eastern Pacific. *Journal of Climate*, **17** (1), 133–139.
- 896 Zhang, C., D. S. Nolan, C. D. Thorncroft, and H. Nguyen, 2008: Shallow Meridional Circu-
897 lations in the Tropical Atmosphere. *Journal of Climate*, **21** (14), 3453–3470, doi:10.1175/
898 2007JCLI1870.1.
- 899 Zheng, X., and E. A. B. Eltahir, 1998: The role of vegetation in the dynamics of West African
900 monsoons. *Journal of Climate*, **11** (8), 2078–2096, doi:10.1175/1520-0442-11.8.2078.

901 LIST OF FIGURES

- 902 **Fig. 1.** The near-surface Saharan Low is indicated at 20°N, the mid-level Saharan High anticyclone
 903 is indicated by at 20°N, and the combination of these is collectively referred to as the Saharan
 904 SMC. The mid-level African Easterly Jet (AEJ), upper-level Tropical Easterly Jet (TEJ), and
 905 upper level anticyclone in the ITCZ are also shown to help orient the reader. 42
- 906 **Fig. 2.** JAS climatological meridional wind v at 14°N for (a) ERA-Interim, and (b) MERRA2.
 907 10°W and 25°E boundaries indicated by black dashed lines. Surface pressure indicated
 908 by a bold red line. 43
- 909 **Fig. 3.** (a) June-September precipitation climatology based on GPCP data, with Sahel and Sahara
 910 boxes indicated. Units mm day^{-1} (b) Detrended interannual time series of anomalous pre-
 911 cipitation over the Sahel box derived from GPCP data, with ± 1 standard deviation bounds
 912 are indicated by dashed lines. (c) Regression slope of local detrended GPCP precipitation
 913 onto Sahel area averaged precipitation in mm day^{-1} per mm day^{-1} . (d) ERA-Interim regres-
 914 sion slope of detrended Z925 ($\text{m mm}^{-1} \text{day}$; colors) and climatological $\Delta Z925$ (dashed con-
 915 tours mark -10 m and -20 m isolines). Statistically significant regression slopes ($p < 0.05$)
 916 are hatched. 44
- 917 **Fig. 4.** Climatological JAS zonal mean (a, b) Divergence (colors; 10^{-6}s^{-1}) and pressure velocity ω
 918 (contours every 0.5 hPa hr^{-1}). (c, d) Zonal wind u (colors) and meridional wind v (contours
 919 every m s^{-1}). ERA-Interim used for panels a and c, whereas MERRA2 is used for panels b
 920 and d. All panels have zero contours omitted, and negative contours are dashed. 45
- 921 **Fig. 5.** All panels use ERA-Interim data. (a, c, e) Colors show climatological JAS Z925, Z700, and
 922 LLAT respectively in units of m . Constant values of 790 m , 3150 m , and 2260 m respectively
 923 were subtracted to reduce them to the same color scale. Arrows show the divergent compo-
 924 nent of the wind \mathbf{u}_χ for the same 925 and 700 hPa levels respectively. (b, d, f) Colors show
 925 the regression slope of detrended Z925, Z700, and LLAT onto GPCP Sahel precipitation
 926 respectively ($\text{m mm}^{-1} \text{day}$), with hatched regions indicating statistical significance. Divergent
 927 wind regression slope for same 925 and 700 hPa levels respectively shown in arrows, with
 928 only regions where u_χ or v_χ is statistically significant and $|\mathbf{u}_\chi| > 0.1 \text{ m s}^{-1} \text{ mm}^{-1} \text{ day}$ are
 929 drawn. 46
- 930 **Fig. 6.** $\Delta Z925$, $\Delta Z700$, and LLAT were averaged over the Sahara and Sahel in both ERA-Interim
 931 and MERRA2 reanalyses, detrended, and regressed against Sahel precipitation. 68% (thick)
 932 and 95% (thin) confidence intervals of the regression slope are shown. Climatological values
 933 of each quantity and the Pearson R coefficient of the regression are indicated on the figure.
 934 Critical R values with $n - 2 = 34$ degrees of freedom are 0.329, 0.423, and 0.525 at the 0.05,
 935 0.01, and 0.001 levels. 47
- 936 **Fig. 7.** Regressions against Sahel precipitation of: (a) 925 hPa trough location (latitude of minimum
 937 925 hPa $\Delta Z925$), (b) Latitude of maximum LLAT, (c) Sahara $\Delta Z925$, and (d) Sahara $\Delta Z925$
 938 with linear dependence on heat low trough location removed. All quantities had the long
 939 term time trend removed after area averaging. 48
- 940 **Fig. 8.** All panels show ERA-Interim zonal averages over 10°W – 25°E . Colors indicate regression
 941 slope of the detrended quantity onto Sahel precipitation, hatching indicates statistical signif-
 942 icance, and black contours indicate climatology (negative dashed, zero omitted). Units on
 943 regression slope imply per mm day^{-1} . (a) θ [K; contours every 5]. (b) ΔZ [meters; contours
 944 every 10]. (c) specific humidity [g kg^{-1} ; contours every 1] (d) u [m s^{-1} ; contours every

945 2]. (e) Horizontal divergence [10^{-6} s^{-1} ; contours every 1]. (f) ω [hPa hr $^{-1}$; contours every
946 0.5]. (g) v [m s^{-1} ; contours every 0.5]. (h) v_χ [m s^{-1} ; contours every 0.5]. 49

947 **Fig. 9.** (a) ERA-Interim climatological vertical integrals of zonally averaged divergence over the
948 specified layers ($10^{-3} \text{ kg m}^{-2} \text{ s}^{-1}$). (b) ERA-Interim regression slope of zonal and vertical
949 integrals of anomalous divergence over the specified layers ($10^{-3} \text{ kg m}^{-2} \text{ s}^{-1} \text{ mm}^{-1} \text{ day}$).
950 Statistically significant slopes are shown in dark, solid colors. (c-d) As in a,b but for
951 MERRA2. 50

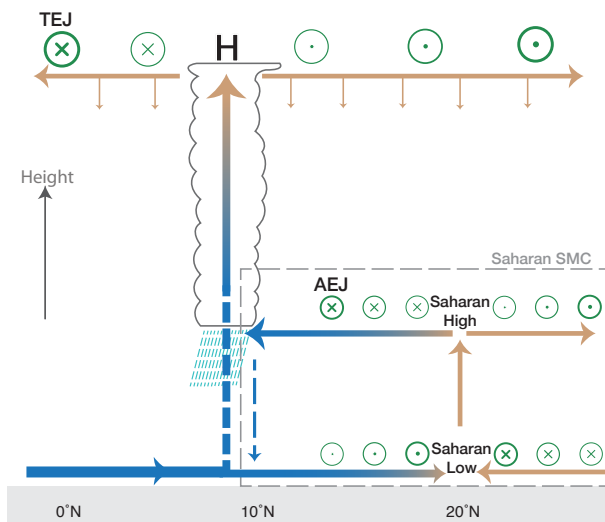
952 **Fig. 10.** (a) Vertically integrated divergence ($10^{-3} \text{ kg m}^{-2} \text{ s}^{-1}$) or layer averaged specific humidity
953 ($10^{-1} \text{ g kg}^{-1}$) detrended and regressed against GPCP Sahel precipitation. 68% (thick) and
954 95% (thin) confidence intervals are shown for the slope of the regression, along with the
955 Pearson R. (b) Regression of detrended upper tropospheric divergence onto detrended mid
956 tropospheric divergence. All quantities are horizontal averages over 10°W – 25°E , 10°N –
957 25°N 51

958 **Fig. 11.** Mass streamfunctions (10^9 kg s^{-1}) ordered by increasing precipitation in the 10° – 20°N box.
959 (a) +2K SST forcing south of Africa. (b) Albedo increase of 0.10 over 12° – 32°N . (c) Control
960 experiment. (d) -2K SST equatorial cold tongue, as in d. (e) Albedo decrease of 0.10 over
961 12° – 32°N 52

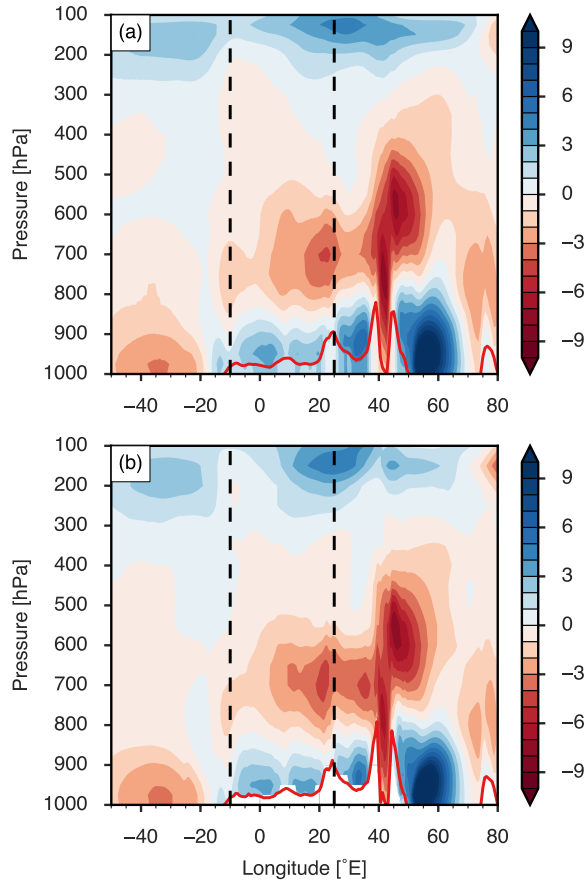
962 **Fig. 12.** (a) The trough location, the latitude of minimum $\Delta Z925$, was calculated and regressed
963 against precipitation. For reanalysis data, it was regressed against detrended GPCP Sa-
964 hel precipitation, and for WRF idealized simulations, it was regressed against model pre-
965 cipitation. (b) The layer integrated divergence ($10^{-3} \text{ kg m}^{-2} \text{ s}^{-1}$) and specific humidity
966 ($10^{-1} \text{ g kg}^{-1}$) were calculated, detrended in reanalyses and regressed against GPCP, or re-
967 gressed against model Sahel precipitation. 68% (thick) and 95% (thin) confidence intervals
968 are shown for the regression slope. For the WRF confidence intervals, Pearson R is shown,
969 and due to a different number of degrees of freedom (11), critical R values are 0.552, 0.683,
970 and 0.800 at the 0.05, 0.01, and 0.001 significance levels. 53

971 **Fig. A1.** ERA-Interim JAS Climatology zonally averaged separately in the western (10°W – 10°E)
972 and eastern (10°E – 25°E) sections of the analysis domain. (a) Divergence (colors; 10^{-6} s^{-1})
973 and pressure velocity ω (contours every 0.5 hPa hr $^{-1}$) averaged over western longitudes.
974 (b) Divergence and pressure velocity over eastern longitudes. (c) Zonal wind u (colors) and
975 meridional wind v (contours every m s^{-1}) over western longitudes. (d) Zonal and meridional
976 wind over eastern longitudes. In all panels, zero contours are omitted, and negative contours
977 are dashed. 54

978 **Fig. A2.** All panels show ERA-Interim zonal averages over 10°W – 10°E (left) or 10°E – 25°E (right).
979 Colors indicate regression slope onto Sahel precipitation, hatching indicates statistical sig-
980 nificance, and black contours indicate climatology (negative dashed, zero omitted). Units
981 on regression slope imply per mm day^{-1} . (a, b) Horizontal divergence [10^{-6} s^{-1} ; contours
982 every 1]. (c, d) ω [hPa hr $^{-1}$; contours every 0.5]. (e, f) u [m s^{-1} ; contours every 2]. (g, h) v
983 [m s^{-1} ; contours every 0.5]. 55



984 FIG. 1. The near-surface Saharan Low is indicated at 20°N, the mid-level Saharan High anticyclone is indi-
 985 cated by at 20°N, and the combination of these is collectively referred to as the Saharan SMC. The mid-level
 986 African Easterly Jet (AEJ), upper-level Tropical Easterly Jet (TEJ), and upper level anticyclone in the ITCZ are
 987 also shown to help orient the reader.



988 FIG. 2. JAS climatological meridional wind v at 14°N for (a) ERA-Interim, and (b) MERRA2. 10°W and
989 25°E boundaries indicated by black dashed lines. Surface pressure indicated by a bold red line.

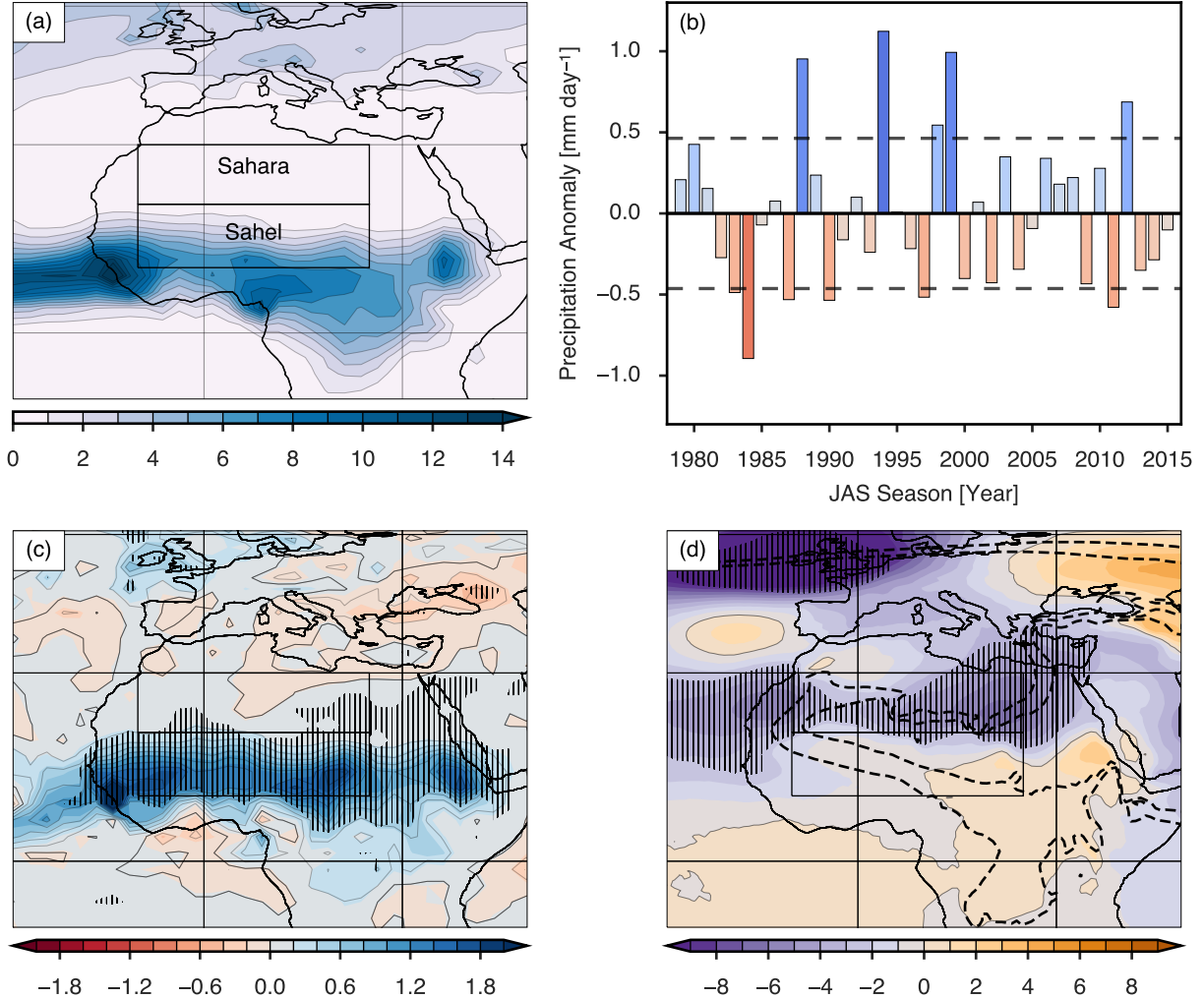


FIG. 3. (a) June-September precipitation climatology based on GPCP data, with Sahel and Sahara boxes indicated. Units mm day^{-1} (b) Detrended interannual time series of anomalous precipitation over the Sahel box derived from GPCP data, with ± 1 standard deviation bounds are indicated by dashed lines. (c) Regression slope of local detrended GPCP precipitation onto Sahel area averaged precipitation in mm day^{-1} per mm day^{-1} . (d) ERA-Interim regression slope of detrended Z925 (m mm^{-1} day; colors) and climatological $\Delta Z925$ (dashed contours mark -10 m and -20 m isolines). Statistically significant regression slopes ($p < 0.05$) are hatched.

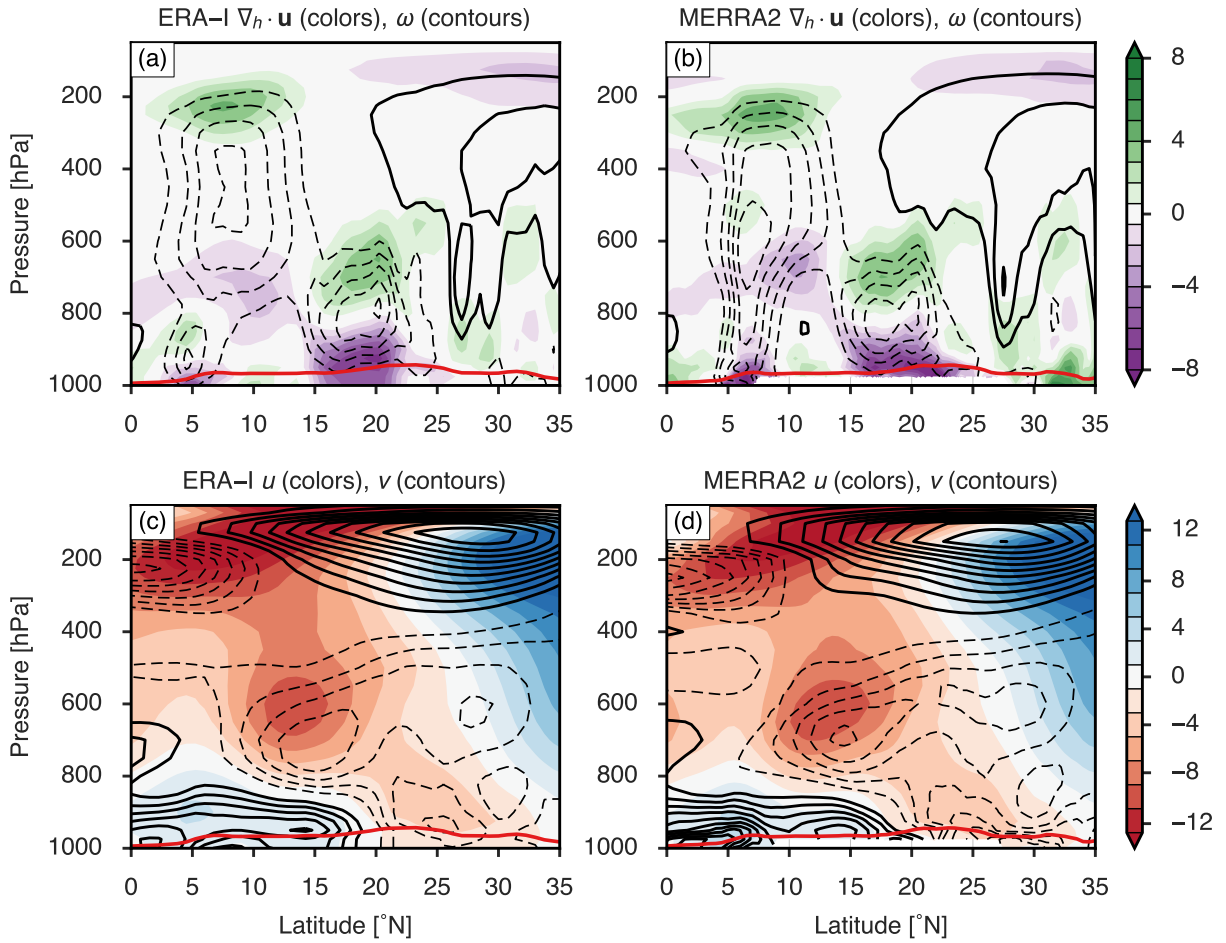


FIG. 4. Climatological JAS zonal mean (a, b) Divergence (colors; 10^{-6} s^{-1}) and pressure velocity ω (contours every 0.5 hPa hr⁻¹). (c, d) Zonal wind u (colors) and meridional wind v (contours every m s^{-1}). ERA-Interim used for panels a and c, whereas MERRA2 is used for panels b and d. All panels have zero contours omitted, and negative contours are dashed.

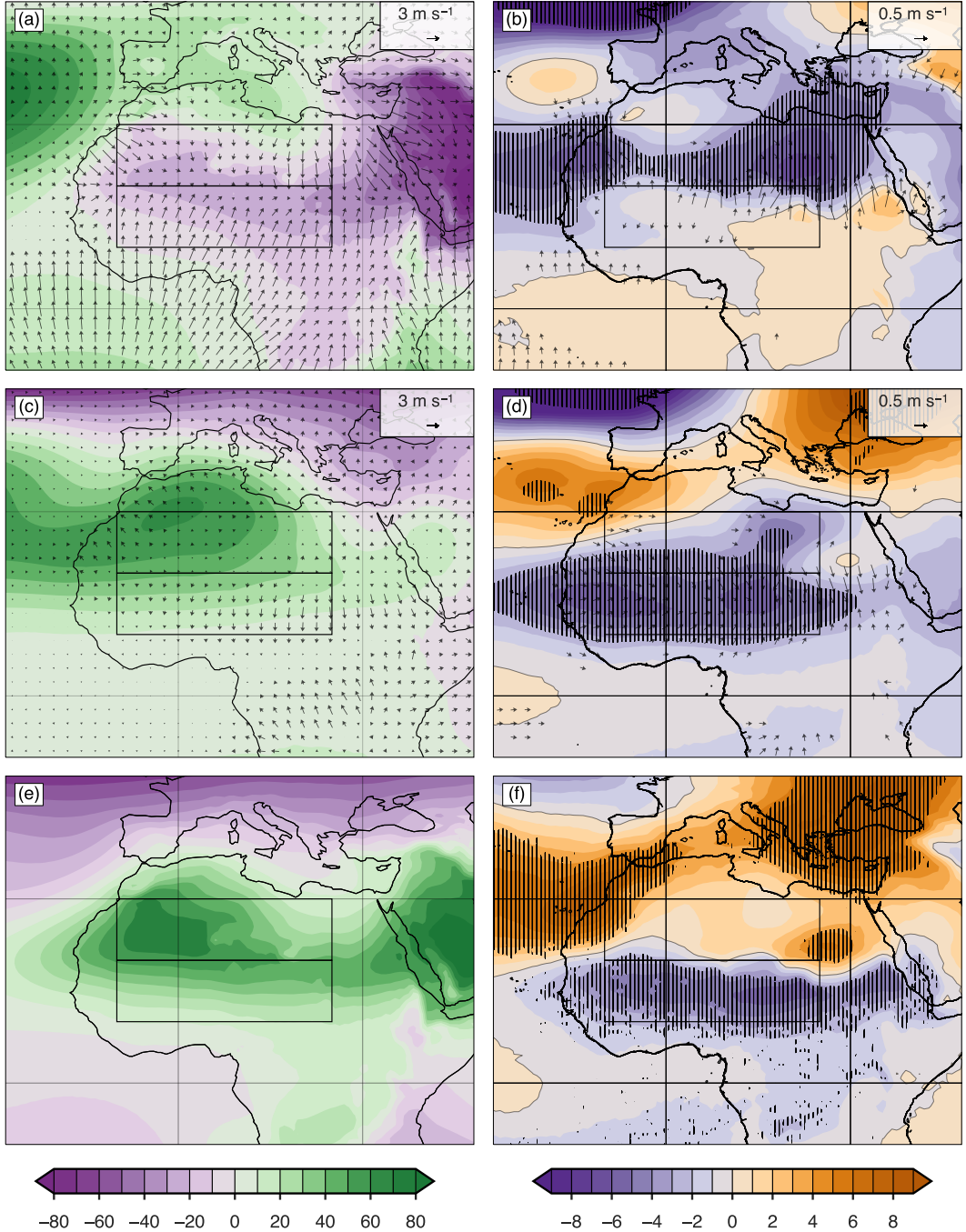
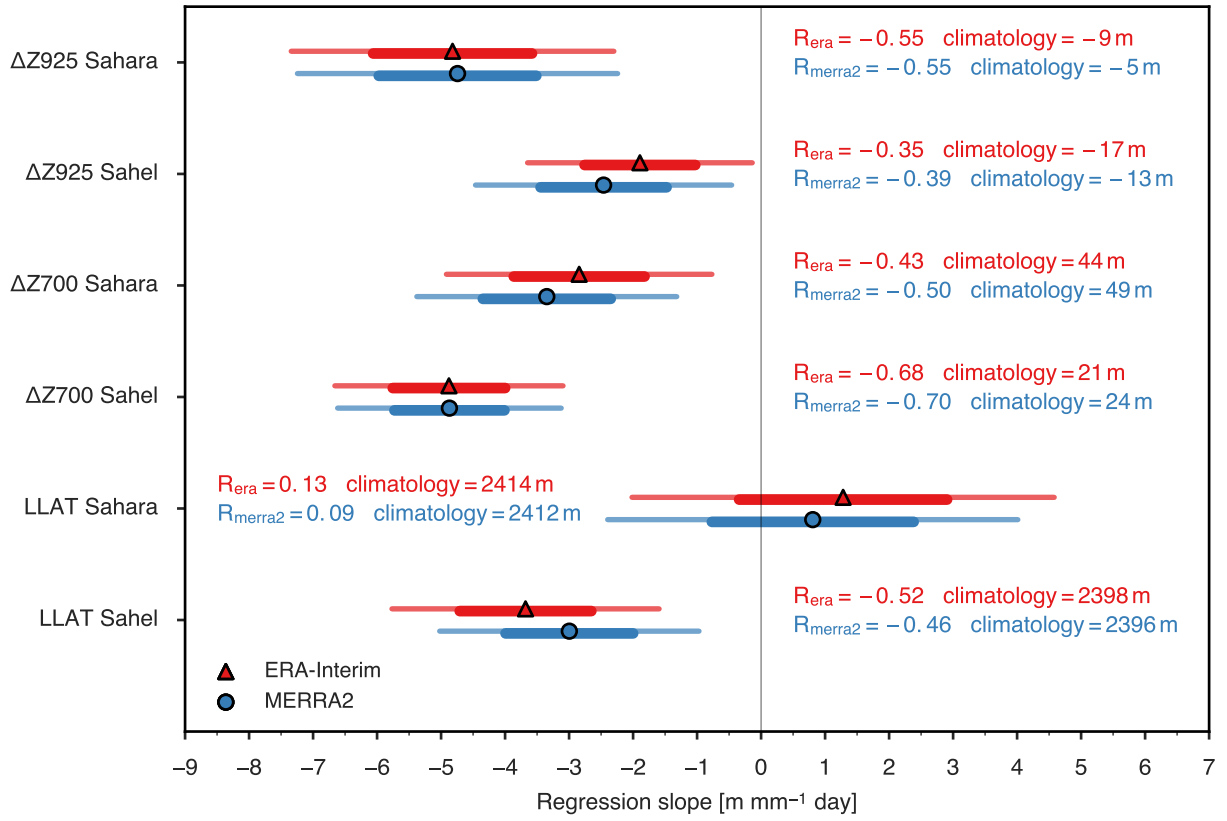


FIG. 5. All panels use ERA-Interim data. (a, c, e) Colors show climatological JAS Z925, Z700, and LLAT respectively in units of m. Constant values of 790 m, 3150 m, and 2260 m respectively were subtracted to reduce them to the same color scale. Arrows show the divergent component of the wind \mathbf{u}_χ for the same 925 and 700 hPa levels respectively. (b, d, f) Colors show the regression slope of detrended Z925, Z700, and LLAT onto GPCP Sahel precipitation respectively ($\text{m mm}^{-1} \text{ day}$), with hatched regions indicating statistical significance. Divergent wind regression slope for same 925 and 700 hPa levels respectively shown in arrows, with only regions where u_χ or v_χ is statistically significant and $|\mathbf{u}_\chi| > 0.47 \text{ m s}^{-1} \text{ mm}^{-1} \text{ day}$ are drawn.



1007 FIG. 6. $\Delta Z925$, $\Delta Z700$, and LLAT were averaged over the Sahara and Sahel in both ERA-Interim and
 1008 MERRA2 reanalyses, detrended, and regressed against Sahel precipitation. 68% (thick) and 95% (thin)
 1009 confidence intervals of the regression slope are shown. Climatological values of each quantity and the Pearson R
 1010 coefficient of the regression are indicated on the figure. Critical R values with $n - 2 = 34$ degrees of freedom
 1011 are 0.329, 0.423, and 0.525 at the 0.05, 0.01, and 0.001 levels.

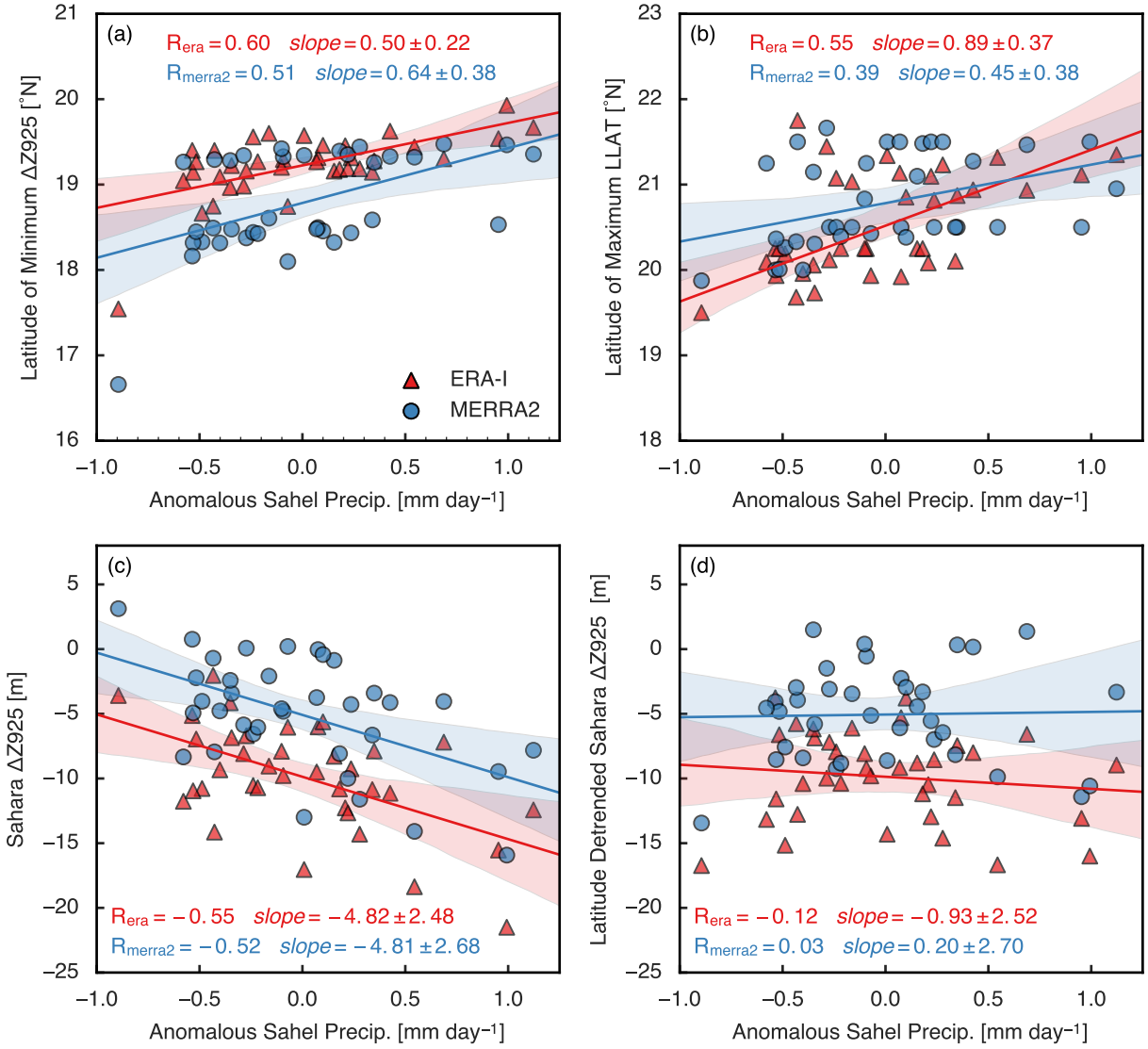


FIG. 7. Regressions against Sahel precipitation of: (a) 925 hPa trough location (latitude of minimum 925 hPa $\Delta Z925$), (b) Latitude of maximum LLAT, (c) Sahara $\Delta Z925$, and (d) Sahara $\Delta Z925$ with linear dependence on heat low trough location removed. All quantities had the long term time trend removed after area averaging.

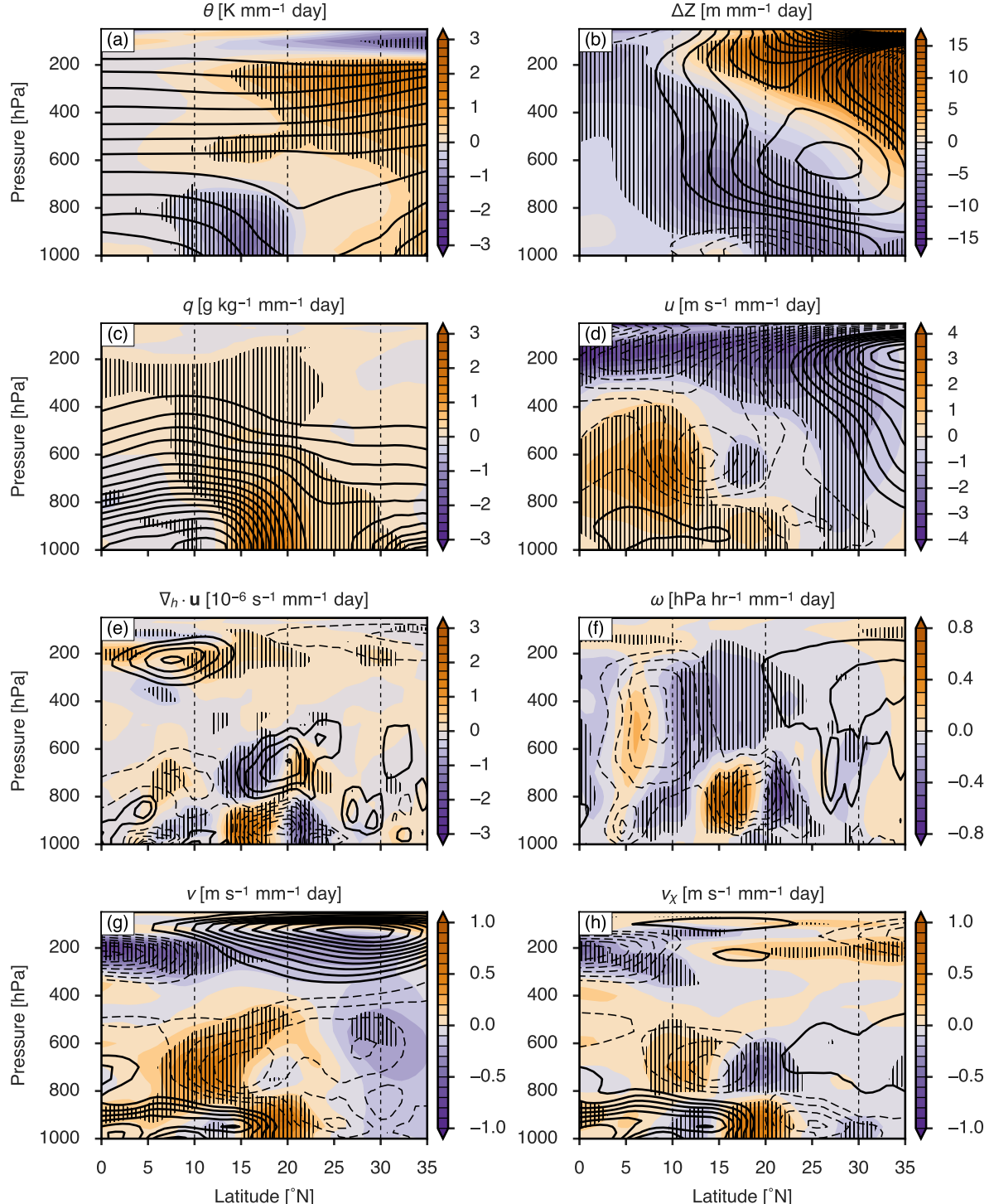


FIG. 8. All panels show ERA-Interim zonal averages over 10°W – 25°E . Colors indicate regression slope of the detrended quantity onto Sahel precipitation, hatching indicates statistical significance, and black contours indicate climatology (negative dashed, zero omitted). Units on regression slope imply per mm day^{-1} . (a) θ [K]; contours every 5]. (b) ΔZ [meters; contours every 10]. (c) specific humidity [g kg^{-1} ; contours every 1] (d) u [m s^{-1} ; contours every 2]. (e) Horizontal divergence $\bar{\rho}\bar{U}^{-6} \text{s}^{-1}$; contours every 1]. (f) ω [hPa hr^{-1} ; contours every 0.5]. (g) v [m s^{-1} ; contours every 0.5]. (h) v_χ [m s^{-1} ; contours every 0.5].

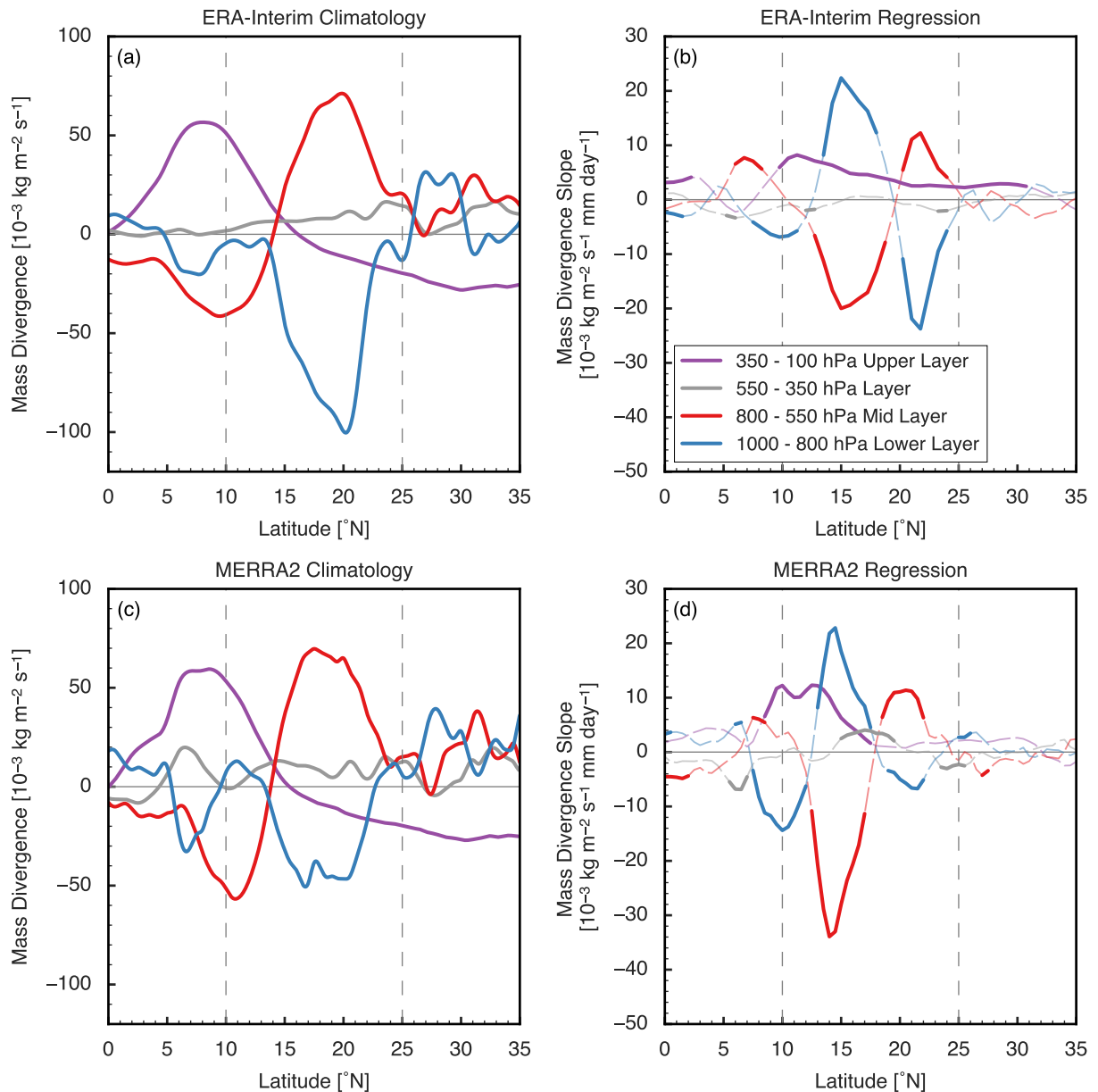


FIG. 9. (a) ERA-Interim climatological vertical integrals of zonally averaged divergence over the specified layers ($10^{-3} \text{ kg m}^{-2} \text{ s}^{-1}$). (b) ERA-Interim regression slope of zonal and vertical integrals of anomalous divergence over the specified layers ($10^{-3} \text{ kg m}^{-2} \text{ s}^{-1} \text{ mm}^{-1} \text{ day}$). Statistically significant slopes are shown in dark, solid colors. (c-d) As in a,b but for MERRA2.

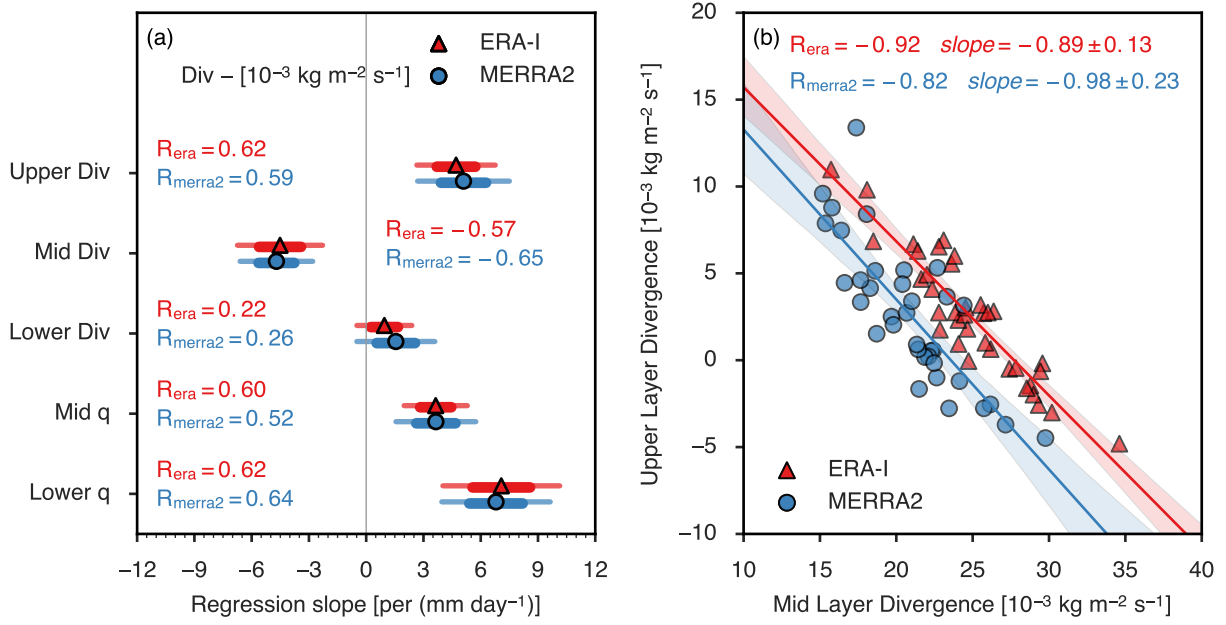


FIG. 10. (a) Vertically integrated divergence ($10^{-3} \text{ kg m}^{-2} \text{ s}^{-1}$) or layer averaged specific humidity ($10^{-1} \text{ g kg}^{-1}$) detrended and regressed against GPCP Sahel precipitation. 68% (thick) and 95% (thin) confidence intervals are shown for the slope of the regression, along with the Pearson R. (b) Regression of detrended upper tropospheric divergence onto detrended mid tropospheric divergence. All quantities are horizontal averages over 10°W – 25°E , 10°N – 25°N .

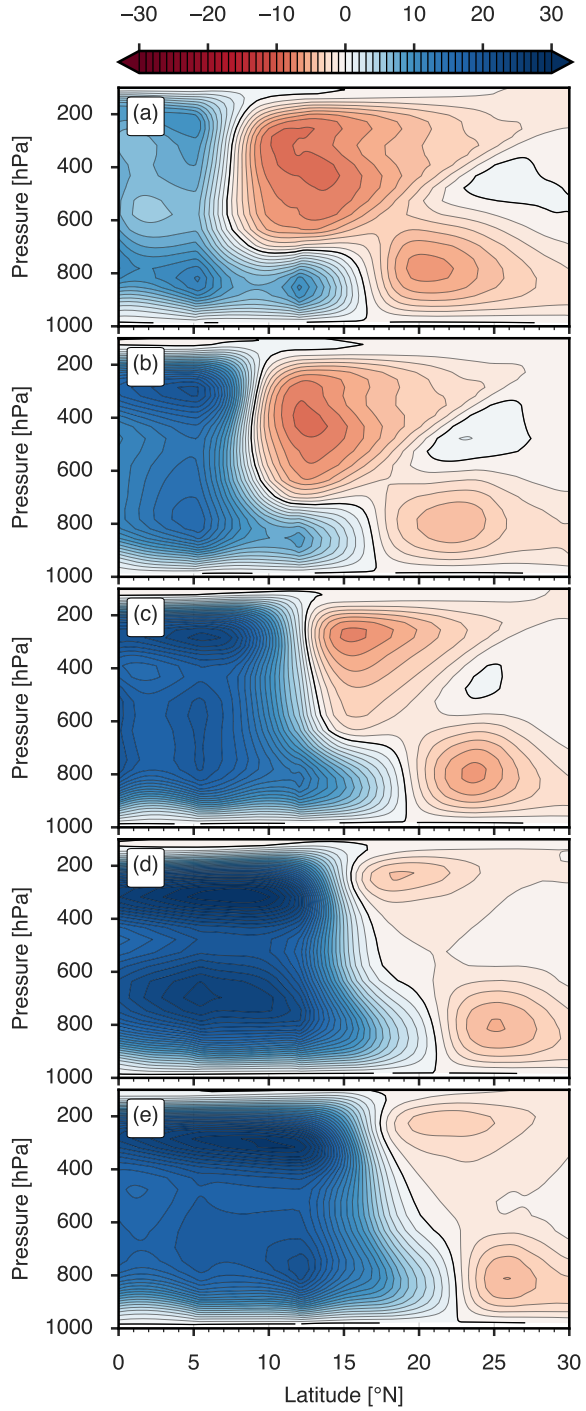


FIG. 11. Mass streamfunctions (10^9 kg s^{-1}) ordered by increasing precipitation in the $10^\circ\text{-}20^\circ\text{N}$ box. (a) +2K
 SST forcing south of Africa. (b) Albedo increase of 0.10 over $12^\circ\text{-}32^\circ\text{N}$. (c) Control experiment. (d) -2K SST
 equatorial cold tongue, as in d. (e) Albedo decrease of 0.10 over $12^\circ\text{-}32^\circ\text{N}$.

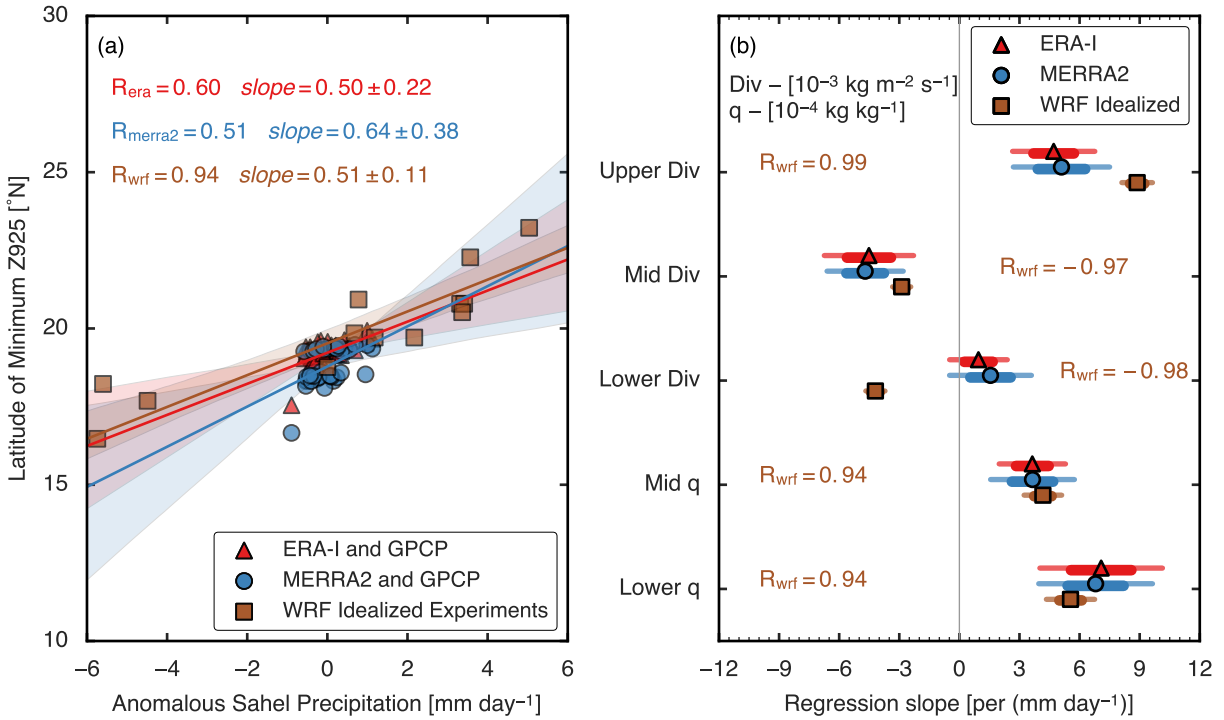


FIG. 12. (a) The trough location, the latitude of minimum $\Delta Z925$, was calculated and regressed against precipitation. For reanalysis data, it was regressed against detrended GPCP Sahel precipitation, and for WRF idealized simulations, it was regressed against model precipitation. (b) The layer integrated divergence ($10^{-3} \text{ kg m}^{-2} \text{ s}^{-1}$) and specific humidity ($10^{-1} \text{ g kg}^{-1}$) were calculated, detrended in reanalyses and regressed against GPCP, or regressed against model Sahel precipitation. 68% (thick) and 95% (thin) confidence intervals are shown for the regression slope. For the WRF confidence intervals, Pearson R is shown, and due to a different number of degrees of freedom (11), critical R values are 0.552, 0.683, and 0.800 at the 0.05, 0.01, and 0.001 significance levels.

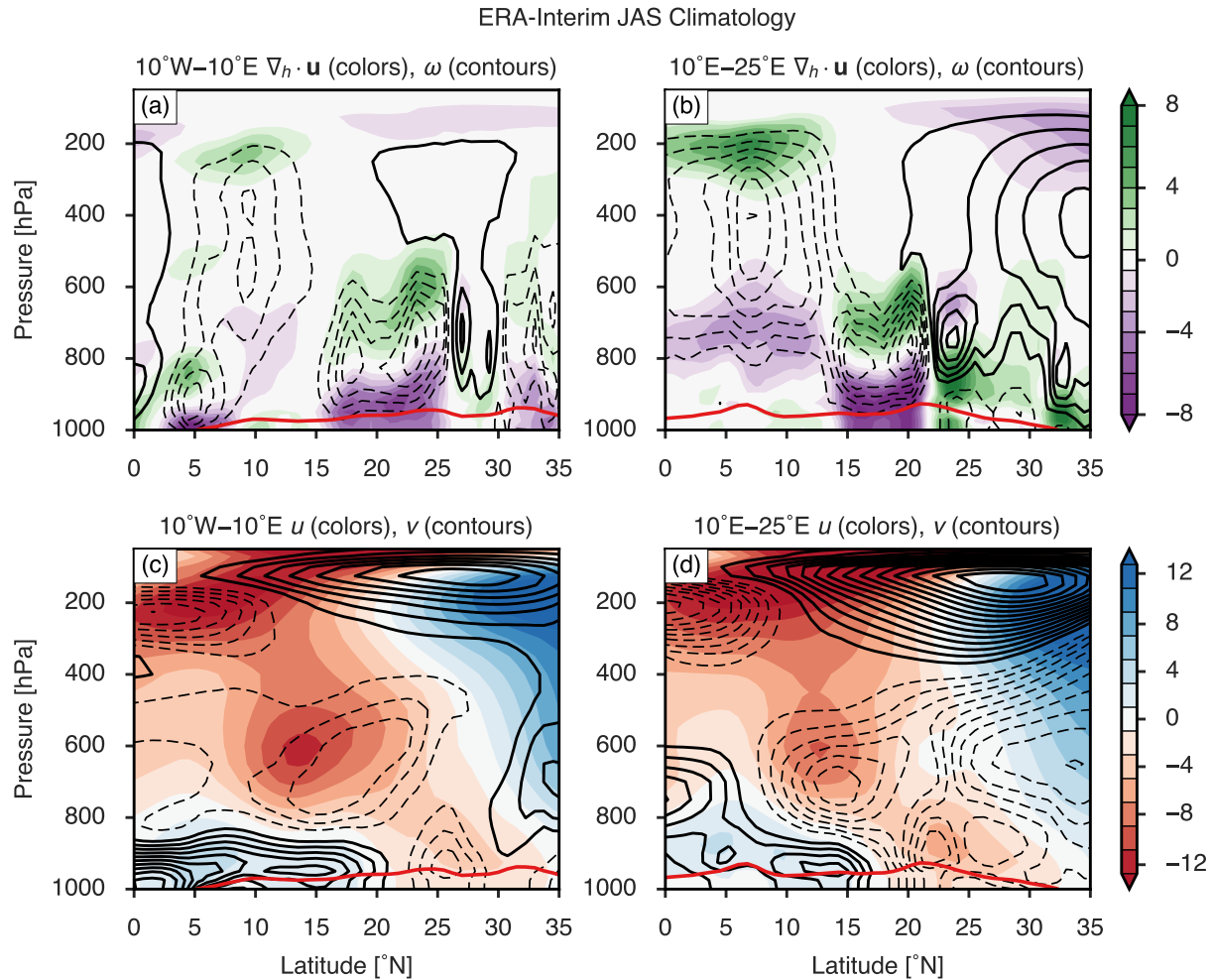
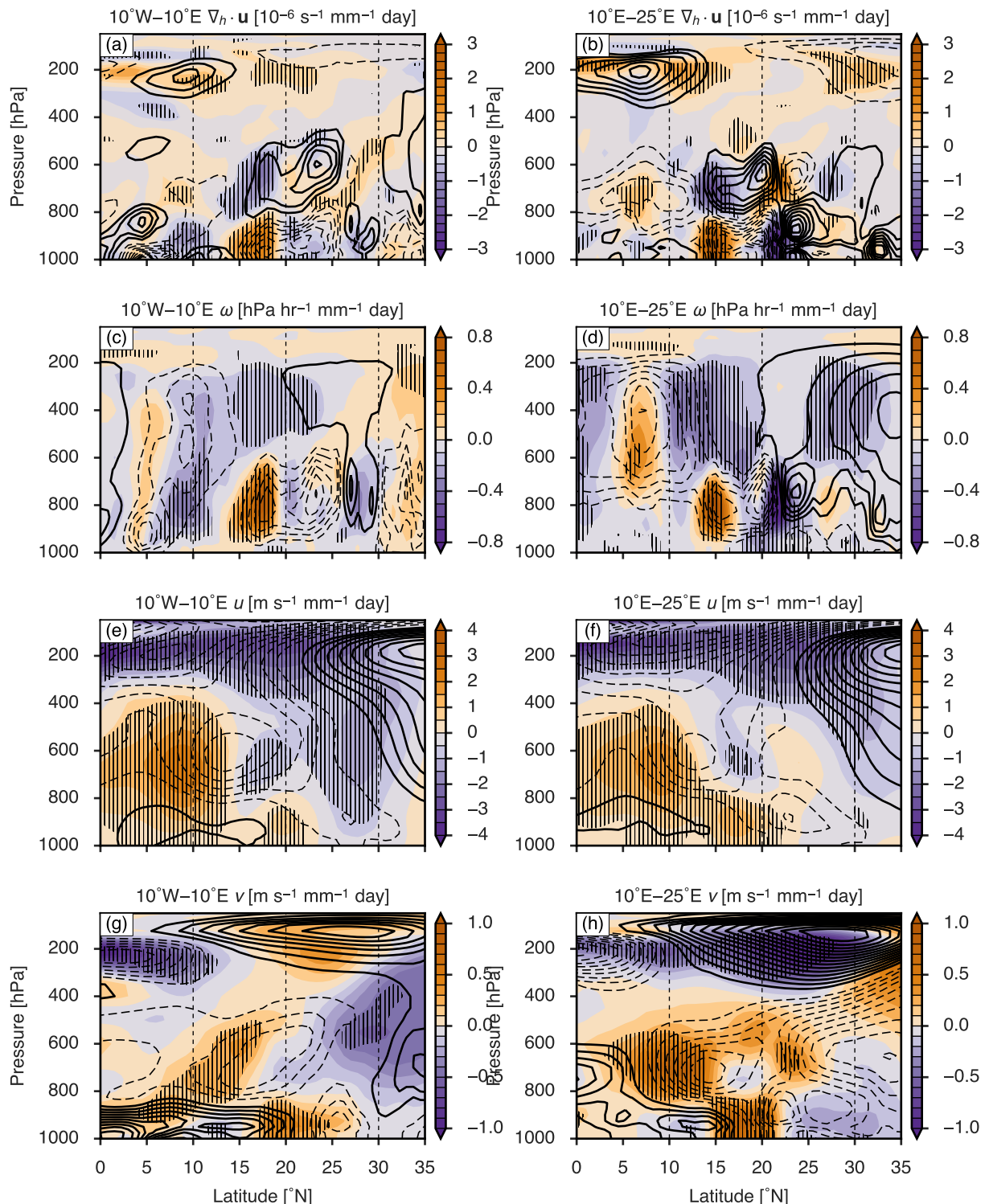


Fig. A1. ERA-Interim JAS Climatology zonally averaged separately in the western ($10^{\circ}\text{W}-10^{\circ}\text{E}$) and eastern ($10^{\circ}\text{E}-25^{\circ}\text{E}$) sections of the analysis domain. (a) Divergence (colors; 10^{-6} s^{-1}) and pressure velocity ω (contours every 0.5 hPa hr^{-1}) averaged over western longitudes. (b) Divergence and pressure velocity over eastern longitudes. (c) Zonal wind u (colors) and meridional wind v (contours every m s^{-1}) over western longitudes. (d) Zonal and meridional wind over eastern longitudes. In all panels, zero contours are omitted, and negative contours are dashed.



1047 Fig. A2. All panels show ERA-Interim zonal averages over 10°W–10°E (left) or 10°E–25°E (right). Colors
 1048 indicate regression slope onto Sahel precipitation, hatching indicates statistical significance, and black contours
 1049 indicate climatology (negative dashed, zero omitted). Units on regression slope imply per mm day^{-1} . (a, b)
 1050 Horizontal divergence [10^{-6} s^{-1} ; contours every 1]. (c, d) ω [hPa hr^{-1} ; contours every 0.5]. (e, f) u [m s^{-1} ;
 1051 contours every 2]. (g, h) v [m s^{-1} mm $^{-1}$ day]; contours every 0.5].